Magnetic flux pileup and plasma depletion in Mercury's subsolar magnetosheath

Daniel J. Gershman,[1,2] James A. Slavin,[1] Jim M. Raines,[1] Thomas H. Zurbuchen,[1] Brian J. Anderson,[3] Haje Korth,[3] Daniel N. Baker,[4] and Sean C. Solomon[5,6]

Received 29 July 2013; revised 24 September 2013; accepted 18 October 2013; published 25 November 2013.

[1] Measurements from the Fast Imaging Plasma Spectrometer (FIPS) and Magnetometer (MAG) on the MErcury Surface, Space ENvironment, GEochemistry, and Ranging spacecraft during 40 orbits about Mercury are used to characterize the plasma depletion layer just exterior to the planet's dayside magnetopause. A plasma depletion layer forms at Mercury as a result of piled-up magnetic flux that is draped around the magnetosphere. The low average upstream Alfvénic Mach number (M_A ~3–5) in the solar wind at Mercury often results in large-scale plasma depletion in the magnetosheath between the subsolar magnetopause and the bow shock. Flux pileup is observed to occur downstream under both quasi-perpendicular and quasi-parallel shock geometries for all orientations of the interplanetary magnetic field (IMF). Furthermore, little to no plasma depletion is seen during some periods with stable northward IMF. The consistently low value of plasma β, the ratio of plasma pressure to magnetic pressure, at the magnetopause associated with the low average upstream M_A is believed to be the cause for the high average reconnection rate at Mercury, reported to be nearly 3 times that observed at Earth. Finally, a characteristic depletion length outward from the subsolar magnetopause of ~300 km is found for Mercury. This value scales among planetary bodies as the average standoff distance of the magnetopause.

Citation: Gershman, D. J., J. A. Slavin, J. M. Raines, T. H. Zurbuchen, B. J. Anderson, H. Korth, D. N. Baker, and S. C. Solomon (2013), Magnetic flux pileup and plasma depletion in Mercury's subsolar magnetosheath, *J. Geophys. Res. Space Physics*, *118*, 7181–7199, doi:10.1002/2013JA019244.

1. Introduction

[2] At a planetary bow shock (BS), the supermagnetosonic solar wind is slowed and heated, forming a downstream magnetosheath (MSH) region of hot and dense plasma. Although the magnetosheath properties immediately downstream of the bow shock are driven by solar wind conditions, the dynamic evolution of magnetosheath plasmas as they flow toward the magnetosphere is important in the understanding of magnetospheric dynamics because it is the plasmas and magnetic fields at the inner boundary of the MSH that interact with a planetary magnetosphere. Studying the plasma environment in the MSH for a large range of solar wind conditions at different planetary bodies is therefore vital for understanding the mechanisms by which the solar wind interacts with solar system objects that have intrinsic magnetic fields. Here, we present the first study of Mercury's magnetosheath plasma environment.

[3] Early hydrodynamic simulations of solar wind incident on planetary magnetospheric systems [*Spreiter et al.*, 1966] predicted that in the subsolar MSH, the plasma density along the stagnation streamline should monotonically increase toward the magnetopause (MP). Hydrodynamics does not account, however, for the interplanetary magnetic field, which is substantially altered and intensified across the BS [*Midgley and Davis*, 1963; *Lees*, 1964] and can become dynamically important. Downstream of the BS, a fast-mode shock front under most conditions, the solar wind plasma is submagnetosonic. Farther, in the vicinity of the stagnation streamline, the flow becomes subsonic and sub-Alfvénic, as the magnetic field drapes around and is compressed against the planetary MP boundary. The compression of magnetic flux led *Zwan and Wolf* [1976] to predict that the compressed field would generate a force that squeezes plasma away from the subsolar region, resulting in a decreasing density near the subsolar MP and the formation of a layer with depleted plasma density, the "plasma depletion layer" (PDL).

[1]Department of Atmospheric, Oceanic and Space Sciences, University of Michigan, Ann Arbor, Michigan, USA.
[2]Geospace Physics Laboratory, NASA Goddard Space Flight Center, Greenbelt, Maryland, USA.
[3]The Johns Hopkins University Applied Physics Laboratory, Laurel, Maryland, USA.
[4]Laboratory for Atmospheric and Space Physics, University of Colorado, Boulder, Colorado, USA.
[5]Department of Terrestrial Magnetism, Carnegie Institution of Washington, Washington, DC, USA.
[6]Lamont-Doherty Earth Observatory, Columbia University, Palisades, New York, USA.

Corresponding author: D. J. Gershman, Geospace Physics Laboratory, NASA Goddard Space Flight Center, Greenbelt, MD 20771, USA. (djgersh@umich.edu)

©2013. American Geophysical Union. All Rights Reserved.
2169-9380/13/10.1002/2013JA019244

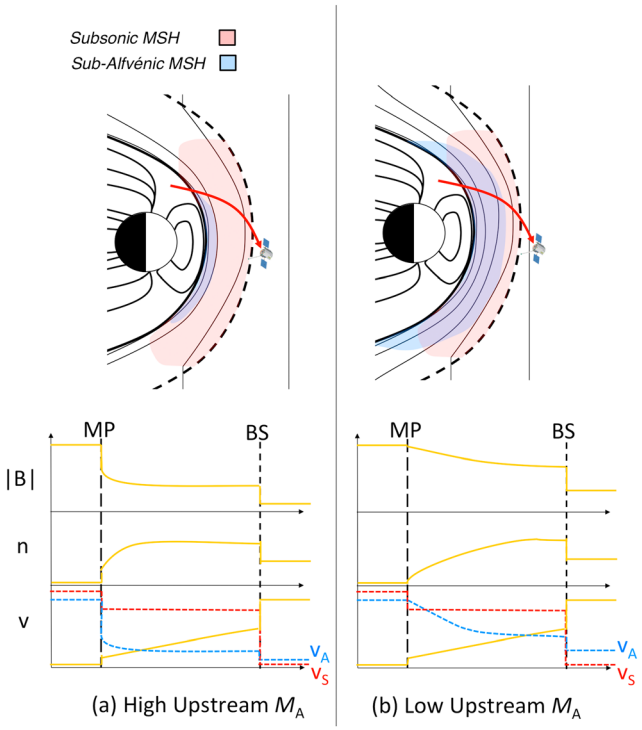

Figure 1. Illustration of a spacecraft pass through the subsolar magnetosheath for (a) high solar wind M_A and (b) low solar wind M_A. The MSH plasma is subsonic equatorward of approximately ±45° latitude. With decreasing M_A, a larger fraction of the subsolar magnetosheath is sub-Alfvénic, as indicated by the blue shaded region. In addition, a thicker region of magnetic flux pileup is evident by an increase in $|\mathbf{B}|$ and a decrease in plasma density, n. The Alfvén speed (V_A) and sound speed (V_S) are also shown for both cases.

[4] For a given size obstacle to the solar wind, *Zwan and Wolf* [1976] argued that the PDL thickness should vary inversely with the square of the upstream Alfvénic Mach number (M_A), as illustrated in Figure 1. For the case of a high M_A, the plasma β — the ratio of plasma pressure to magnetic pressure — downstream of the BS is high, i.e., the plasma pressure dominates the magnetic pressure, and the plasma is fluid-like. Here, the draped field piles up only in a small region near the MP. For the case of low M_A, in contrast, the plasma β downstream of the BS is low, and the magnetic pressure increases over a large region in the MSH. The depletion of plasma also increases the local Alfvén speed, resulting in a larger fraction of the subsolar magnetosheath with sub-Alfvénic flow speeds.

[5] PDLs have long been observed at Earth [*Cummings and Coleman*, 1968; *Crooker et al.*, 1979; *Fuselier et al.*, 1991; *Anderson and Fuselier*, 1993; *Paschmann et al.*, 1993; *Song et al.*, 1993; *Anderson et al.*, 1994, 1997; *Phan et al.*, 1994, 1997; *Farrugia et al.*, 1997; *Moretto et al.*, 2005] leading to updated theoretical predictions [*Southwood and Kivelson*, 1992, 1995] and the successful reproduction of the phenomena with magnetohydrodynamic (MHD) simulations that take into account both magnetic field and hydrodynamic effects [*Lyon*, 1994; *Denton and Lyon*, 2000; *Siscoe et al.*, 2002; *Erkaev et al.*, 2003; *Wang et al.*, 2003, 2004; *Nabert et al.*, 2013]. Plasma depletion is a general process and occurs any time that magnetic flux is draped and compressed against an obstacle as demonstrated in studies of flux pileup and plasma depletion at Venus [*Luhmann*, 1986; *Zhang et al.*, 1991], Mars [*Bertucci et al.*, 2003a; *Øieroset et al.*, 2004], Saturn [*Slavin et al.*, 1983; *Violante et al.*, 1995], and even in the sheath of interplanetary coronal mass ejections [*Liu et al.*, 2006a].

[6] The formation of PDLs is a consequence of the dynamic balance between magnetic flux pileup and subsolar magnetic reconnection, which corresponds to a flow of plasma inward through the magnetopause that serves to transport magnetic flux away from the subsolar region. The occurrence of plasma depletion therefore provides insight into the intensity of flux transport via magnetic reconnection. However, plasma depletion also acts to promote magnetic reconnection, because compared with the near-BS sheath, PDLs have a reduced plasma β and increased Alfvén speed, leading to higher magnetic reconnection rates [*Slavin and Holzer*, 1979; *Scurry et al.*, 1994]. At Earth, these layers typically form during periods of extended northward interplanetary magnetic field (IMF) [*Song et al.*, 1990; *Phan et al.*, 1994; *Anderson et al.*, 1997]. They have also been observed, however, during periods of southward IMF with high upstream Alfvénic Mach numbers (~8–10) [*Anderson et al.*, 1997] or high plasma density [*Moretto et al.*, 2005] in which the high plasma β inhibits reconnection despite a thin magnetic barrier. Flux pileup and plasma depletion have rarely been studied in the low M_A (3–5) regime. Such events are observed primarily during the impact of large coronal mass ejection on a magnetosphere [*Farrugia et al.*, 1995]. *Farrugia et al.* [1995] found that PDL formation is possible under low M_A even if the IMF is southward because of the extremely thick magnetic barrier region.

[7] Compared with the situation at Earth and the outer planets, at Mercury the average upstream M_A is lower and the solar wind forcing is stronger [*Baker et al.*, 2013]. In addition, Mercury's magnetosphere is smaller relative to both the planet's radius and key plasma scale lengths, and it exhibits higher MP reconnection rates [*Slavin et al.*, 2009; *DiBraccio et al.*, 2013]. The magnetosheath conditions at Mercury, both as imposed at the outer boundary by the solar wind and at the magnetopause, are seldom experienced elsewhere in the solar system. Studying magnetosheath plasma depletion at Mercury can thus reveal key dynamics of flux pileup in a low-β MSH environment. Here, we present the first study of plasma depletion at Mercury, using data from the Magnetometer (MAG) instrument [*Anderson et al.*, 2007] and Fast Imaging Plasma Spectrometer (FIPS) sensor [*Andrews et al.*, 2007] on the MErcury Surface, Space ENvironment, GEochemistry, and Ranging (MESSENGER) spacecraft [*Solomon et al.*, 2001].

[8] In the next section, we introduce a new method for the determination of plasma parameters that results in estimates of density and temperature for the partial particle distribution functions measured by FIPS, given its partially obstructed view from behind MESSENGER's sunshade. These parameters can be recovered in subsonic regions of Mercury's space environment. We then apply the Rankine-Hugoniot shock jump conditions across Mercury's bow shock to the MAG and FIPS data to infer upstream M_A values for selected orbits.

In the subsequent section, we apply the FIPS-derived plasma parameters in conjunction with magnetic field data from MAG to investigate magnetic flux pileup and plasma depletion in Mercury's magnetosheath. Finally, we offer a synthesis of these results with observations of plasma depletion at other planetary bodies.

2. Plasma Parameters From FIPS

[9] FIPS is a time-of-flight (TOF) mass spectrometer that measures the mass-per-charge (m/q) and energy-per-charge (E/q) ratios of incident ions. The novel electrostatic analyzer (ESA) design enables instantaneous field-of-view (FOV) imaging of ~1.4π sr about its boresight direction. The arrival direction of ions is mapped with an angular resolution of ~15° using a position-sensing anode. The spacecraft sunshade and other parts of the structure partially obstruct the FIPS detector, so the instantaneous FOV is approximately 1.15π sr. The TOF measurement allows separation of m/q between 1 and 40 amu/e. For the data presented here, the sensor stepped from 46 eV/e to 13.7 keV/e in 60 logarithmically spaced E/q steps with an integration time of 50 ms at each step and a total scanning time of ~ 10 s. Data from only E/q steps greater than 100 eV/e were used in this study. For TOFs corresponding to H^+, the distributions of particle detection rate versus E/q were calculated onboard to conserve telemetry downlink volume. These rate-energy spectra are used here because they are available continuously, whereas three-dimensional proton distributions are telemetered only sporadically. A more complete description of FIPS operation and its capabilities has been given by *Andrews et al*. [2007].

2.1. Density and Temperatures Estimates for Subsonic Plasmas

[10] Since the solid angle detected by FIPS is less than one third of the ideal 4π sr corresponding to a full view of all arrival directions, we applied an inversion method to recover moment estimates from partially observed distributions. Techniques that use spherical harmonics or other fitting functions to match measured data have been successfully used to derive plasma properties from partially observed distribution functions [*Feldman et al*., 1975; *Pilipp et al*., 1987; *Maksimovic et al*., 1997, 2005; *Skoug et al*., 2000; *Nieves-Chinchilla and Viñas*, 2008; *Viñas and Gurgiolo*, 2009]. Here, we use partial plasma moments to recover estimations of plasma density and temperature from E/q spectra only. We assume only subsonic flow and near-isotropy. An analogous technique was used by *Gershman et al*. [2012] to recover velocity and temperature estimates from E/q energy spectra under the assumption of supersonic flow. We build upon the method used by *Raines et al*. [2011] and *Zurbuchen et al*. [2011], by which E/q spectra corresponding to a series of isotropic, stationary Maxwellian distributions with varying plasma density (n) and temperature (T) were generated from an instrument forward model of FIPS and then matched to orbital observations. This new moment-based approach enables recovery of n and T from measured data at high cadence without fitting.

[11] From *Raines et al*. [2011], the conversion between plasma phase space density (f) and the number of measured counts at the ith E/q step (N_i) as a function of particle speed (v_i) is

$$N_\text{i} = \frac{1}{\pi}\cdot v_\text{i}^4 \cdot f(v_\text{i},\theta,\varphi)\cdot g_\text{i}\cdot \varepsilon_\text{i}\cdot \Delta t\cdot \sin(\theta)\Delta\theta\Delta\varphi \tag{1}$$

[12] Here, g_i is the geometric factor of the ESA, ε_i is the combined efficiency of the particle detectors, Δt is the time accumulation per energy step, and $\sin(\theta)\Delta\theta\Delta\varphi$ is the solid angle of incident particles over which the counts are accumulated at polar angle θ and clock angle φ. All quantities are in the instrument frame with $\theta_\text{FIPS} = 0°$ corresponding to the FIPS boresight vector. For an individual event, $\sin(\theta)\Delta\theta\Delta\varphi$ corresponds to the solid angle that maps to the appropriate detector pixel on the position-sensing anode. Because we use proton rate spectra instead of individual events, the solid angle of interest is the total integrated FOV, $\Delta\Omega \approx 1.15\pi$ sr.

[13] Because N_i is a strongly increasing function of v_i, there is a velocity threshold, v_min, below which the average counts per integration time is less than unity, i.e., $N_\text{i} < 1$. Except for very dense or cool plasmas, the energy spectrum will exhibit a low-energy cutoff that could be misinterpreted as a signature of an accelerated or flowing distribution, when in actuality the plasma is Maxwellian and nearly stagnant. To avoid this ambiguity in our analysis, the velocity threshold (v_min) for a particular distribution is specifically identified as the lowest energy-per-charge step for which there is at least one other measured event within three adjacent E/q channels. The velocity corresponding to the highest energy-per-charge step of the sensor is denoted as v_max, and only channels with incident velocities between v_min and v_max are used to estimate phase space density following equation 1.

[14] The velocity distribution in units of s^3m^{-6} of an isotropic Maxwellian with zero bulk velocity ($v_\text{o} = 0$) in the FIPS instrument frame with density n_o, and temperature T is

$$f(v,\theta,\varphi) = n_\text{o}\left(\frac{1}{2\pi}\right)^{3/2}\left(\frac{1}{v_\text{th}^3}\right)\exp\left(-\frac{v^2}{2v_\text{th}^2}\right) \tag{2}$$

[15] Here, the thermal velocity is defined as $v_\text{th} \equiv \sqrt{k_\text{B}T/m}$, where k_B is Boltzmann's constant and m is the mass of the particle. The plasma parameters n_o and T can be recovered by taking moments of a distribution function in spherical coordinates using

$$n_\text{o} = \Delta\Omega\int_0^\infty f(v,\theta,\varphi)\cdot v^2 dv, \tag{3}$$

and

$$v_\text{th}^2 = \frac{\Delta\Omega}{n_\text{o}}\int_0^\infty v^2 f(v,\theta,\varphi)\cdot v^2 dv. \tag{4}$$

[16] These moments must be rewritten in terms of the velocity range and angular FOV of FIPS. Here, we first denote the observed E/q distribution function integrated over the FIPS FOV as f_obs, in units of $s^{-3}\,m^{-6}$ sr, i.e.,

$$f_\text{obs}(v) \equiv \iint_{\Delta\Omega} f(v,\theta,\varphi)d\Omega. \tag{5}$$

[17] We then integrate equations 3 and 4 from $v_{\min}$ to $v_{\max}$ and over the actual angular FIPS FOV, $\Delta\Omega \approx 1.15\pi$ sr. This integration yields the following relationships between moments of f_{obs} and the plasma parameters n_{o} and T,

$$\int_{v_{\min}}^{v_{\max}} f_{\text{obs}}(v)\cdot v^2 dv = \Delta\Omega\cdot n_{\text{o}}\left(\frac{1}{2\pi}\right)^{3/2}\left(\frac{1}{v_{\text{th}}^3}\right)\cdot\left[\begin{array}{l}\sqrt{\frac{\pi}{2}}v_{\text{th}}^3\left(\text{erf}\left(\frac{v_{\max}}{\sqrt{2}v_{th}}\right)-\text{erf}\left(\frac{v_{\min}}{\sqrt{2}v_{\text{th}}}\right)\right)\\ -\exp\left(-\frac{v_{\max}^2}{2v_{\text{th}}^2}\right)\left(v_{\text{th}}^2 v_{\max}\right)\\ +\exp\left(-\frac{v_{\min}^2}{2v_{\text{th}}^2}\right)\left(v_{\text{th}}^2 v_{\min}\right)\end{array}\right] \tag{6}$$

and

$$\int_{v_{\min}}^{v_{\max}} v^2 f_{\text{obs}}(v)\cdot v^2 dv = \Delta\Omega\cdot n_{\text{o}}\left(\frac{1}{2\pi}\right)^{3/2}\left(\frac{1}{v_{\text{th}}^3}\right)\cdot\left[\begin{array}{l}3\sqrt{\frac{\pi}{2}}v_{\text{th}}^5\left(\text{erf}\left(\frac{v_{\max}}{\sqrt{2}v_{th}}\right)-\text{erf}\left(\frac{v_{\min}}{\sqrt{2}v_{\text{th}}}\right)\right)\\ -\exp\left(-\frac{v_{\max}^2}{2v_{\text{th}}^2}\right)\left(3v_{\text{th}}^4 v_{\max}+v_{\text{th}}^2 v_{\max}^3\right)\\ +\exp\left(-\frac{v_{\min}^2}{2v_{\text{th}}^2}\right)\left(3v_{\text{th}}^4 v_{\min}+v_{\text{th}}^2 v_{\min}^3\right)\end{array}\right] \tag{7}$$

where erf is the error function. Here, f_{obs} is implicitly assumed to be isotropic since the solid angle integral becomes a scalar, $\Delta\Omega$. With known f_{obs}, $\Delta\Omega$, $v_{\min}$, and $v_{\max}$, equations 6 and 7 form a system of equations that can be solved numerically to obtain estimates of n_{o} and T.

[18] This recovery of plasma parameters was tested with synthetic data from the FIPS forward model used by *Raines et al*. [2011] and *Zurbuchen et al*. [2011], and a detailed analysis of errors associated with this inversion method is presented in Appendix A. For a broad range of bulk plasma flows ($v_{\text{o}}/v_{\text{th}} \lesssim 0.5$) and temperature ratios ($0.5 \lesssim T_{\perp}/T_{\parallel} \lesssim 5$), where $T_{\parallel}$ and $T_{\perp}$ are the plasma temperature along and perpendicular to the direction of the local magnetic field, respectively, the recovery error primarily scales inversely with the total number of counts in an *E/q* distribution. The relative density and temperature errors scale as $7.02\,N^{-0.96}$ and $1.10\,N^{-0.64}$, respectively. Density errors for plasmas will increase with higher flow speeds, i.e., $v_{\text{o}}/v_{\text{th}} > 0.5$. However, for the special case of a bulk flow nearly perpendicular to the FIPS boresight direction, the accumulation of such a distribution over the wide FIPS FOV results in low recovery errors (<20%) that are nearly independent of plasma flow speed (Appendix A).

[19] As an example recovery, Figure 2 shows recovered density and temperature for a MESSENGER magnetospheric transit for which the spacecraft traversed the nightside plasma sheet and the subsolar magnetosheath. Both of these regions are expected to contain plasmas that are highly subsonic. The plasma sheet is hot and tenuous with $n_{\text{p}} \sim 5\,\text{cm}^{-3}$ and $T_{\text{p}} \sim 10$ MK, and the magnetosheath is cooler and denser with $n_{\text{p}} \sim 100\,\text{cm}^{-3}$ and $T_{\text{p}} \sim 2$ MK. Because of the higher temperature and lower density of the plasma sheet, the measured flux appears misleadingly peaked in energy per charge. However, the number of measured events in each scan is high (i.e., $N > 100$), leading to low expected plasma parameter recovery errors.

[20] The proton thermal pressure was multiplied by 1.1 to account for the partial pressure of He^{2+}, which should have an abundance of 1–4% and a temperature up to 4 times that of the protons [*Fuselier et al*., 1991]. Electron and other heavy ion thermal pressures are neglected because of their low expected temperatures and small abundances, respectively [*Paschmann et al*., 1993; *Phan et al*., 1994; *Wang et al*., 2012]. Not only are the recovered densities and temperatures consistent with expectations of plasma parameters for these regions, but the calculated plasma thermal pressures approximately account for the diamagnetic depression observed in the magnetic field measurements in the plasma sheet and the jump in the magnetic field magnitude at the MP [*Korth et al*., 2011].

[21] As shown in Figure 2, density and temperature are estimated in the magnetosheath only from the MP to 75% of the distance to the BS. This restriction is enforced to minimize effects of downstream plasma flow and BS dynamics on the recovered parameters. In addition, bursty flows that can accompany flux transfer events [*Slavin et al*., 2012] or boundary crossings that occur during a fraction of a FIPS energy-per-charge scan time [*DiBraccio et al*., 2013] can lead to an erroneous recovery. Such events must be analyzed in detail and are excluded here. Further difficulties arise in analysis of cusp-like plasmas, which may exhibit substantial directional anisotropy due to precipitation loss to the planetary surface.

2.2. Estimates of Upstream Solar Wind Speeds

[22] Solar wind speeds and temperatures for multiple ion species are intermittently available from FIPS observations outside of Mercury's bow shock [*Gershman et al*., 2012]. However, these parameters are not necessarily recoverable for every orbit and are a strong function of spacecraft orientation. Fortunately, observations made in the flanks of Mercury's magnetosheath present another opportunity to estimate the solar wind bulk speed. In these regions, the plasma is substantially heated, but only slightly slowed [*Spreiter et al*., 1966], resulting in a plasma that is easily observable by FIPS nearly independent of spacecraft orientation. In the example shown in Figure 3, a MESSENGER crossing of the bow shock in the magnetosheath flank, the measured flux substantially increased, but the derived flow speed was reduced only by approximately 15%, consistent with expectations from hydrodynamic shock theory [*Spreiter et al*., 1966]. When solar wind speeds are not directly recoverable outside of the bow shock we estimate the upstream solar wind speed from magnetosheath-recovered values by multiplying the sheath flow speed by 1.15.

2.3. Estimates of Upstream M_{A}

[23] The plasma density is not directly recoverable from FIPS observations outside the bow shock or inside the flanks of the magnetosheath. However, we can estimate the upstream solar wind dynamic pressure from the Rankine-Hugoniot shock jump conditions and combined FIPS and MAG observations made in the subsolar magnetosheath. Given a static, planar shock geometry, we use the subscripts "n" and "t" to

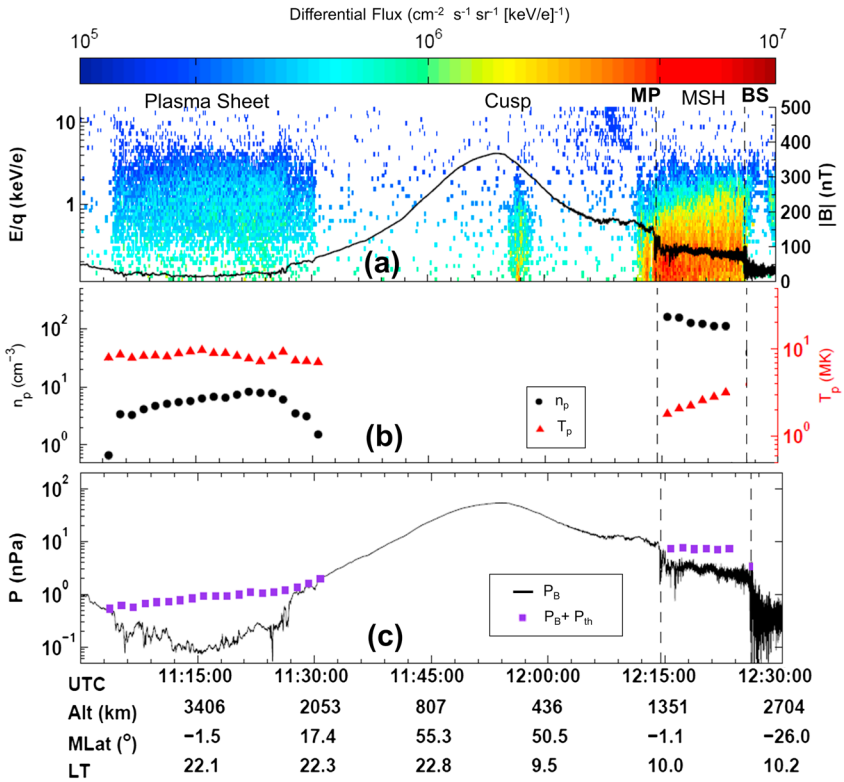

Figure 2. (a) Energy-per-charge spectrogram of the H^+ flux for a MESSENGER magnetospheric transit on 22 February 2012. The magnetic field magnitude from MAG is also shown. (b) Recovered density and temperature for 2 min averages of FIPS energy-per-charge scans. (c) Magnetic and total pressure calculated from MAG and FIPS data. The total pressure was calculated from magnetic field magnitude measurements averaged over the FIPS energy-per-charge scanning time. The plasma thermal pressure accounts for the depression of magnetic pressure in the plasma sheet and the change in magnetic field magnitude across the MP boundary.

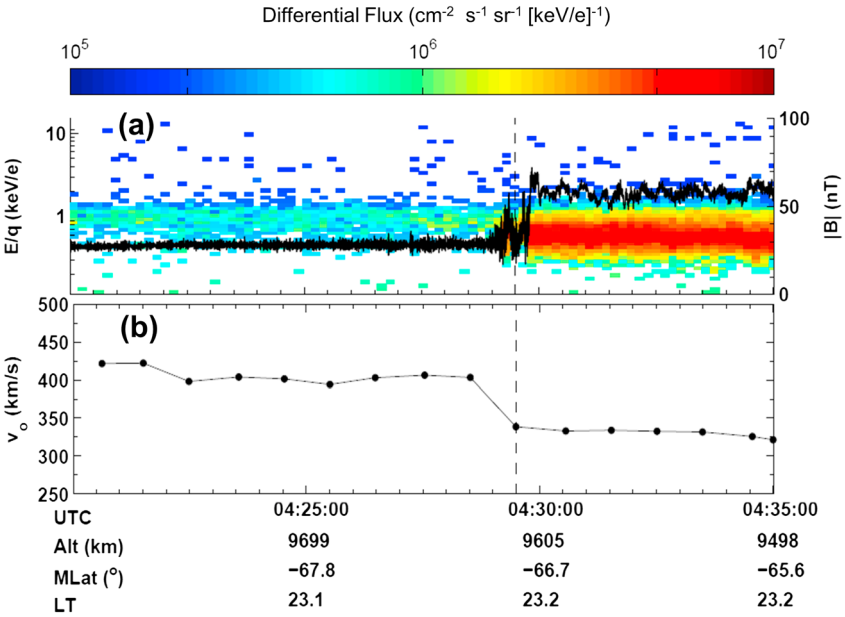

Figure 3. (a) Energy-per-charge spectrogram of FIPS-measured H^+ flux for a MESSENGER BS crossing in the MSH flank on 10 August 2012. The magnetic field magnitude from MAG is also shown. (b) Estimates of the velocity of the solar wind and MSH plasma using the recovery method of *Gershman et al*. [2012] applied to 1 min averages of plasma data. Inside the MSH, the bulk speed is reduced by approximately 15% relative to the solar wind speed.

denote the normal and tangential components of vectors with respect to the shock, respectively. Quantities observed directly upstream and downstream of the shock are denoted with subscripts "u" and "d", respectively.

[24] The shock normal, $\hat{\boldsymbol{n}}$, and shock angle, θ_{BN}, can be computed from three-dimensional upstream and downstream velocity and magnetic field measurements [*Abraham-Shrauner*, 1972]. Because three-dimensional plasma velocity is not available on both sides of the shock, we are limited to using magnetic field data only. However, shock angles calculated from only magnetic field data tend to suffer from large uncertainties [*Schwartz*, 1998]. Therefore, for the analysis presented here, θ_{BN} is calculated using the surface model normal direction [*Slavin et al.*, 1980] as determined by *Winslow et al.* [2013] and a 1 min average of the IMF upstream of the bow shock (B_{u}).

[25] With a measured $\mathbf{B_u}$ from MAG and a model shock normal, $\hat{\boldsymbol{n}}$, the component of the magnetic field normal to the shock, B_{n}, can be computed:

$$B_{\mathrm{n}} = \boldsymbol{B}_{\mathrm{u}} \cdot \hat{\boldsymbol{n}} \tag{8}$$

[26] Since B_{n} is constant across the shock, the tangential components can be found using B_{n} and 1 min averages of field magnitude on either side of the bow shock, B_{u} and B_{d}

$$B_{\mathrm{ut}} = \sqrt{|B_{\mathrm{u}}|^2 - B_{\mathrm{n}}^2}, \tag{9a}$$

and

$$B_{\mathrm{dt}} = \sqrt{|B_{\mathrm{d}}|^2 - B_{\mathrm{n}}^2}. \tag{9b}$$

[27] Applying the Rankine-Hugoniot shock jump conditions, we can use the measured magnetic field from MAG and measured downstream thermal pressure (p_{d}) from FIPS to estimate the upstream solar wind dynamic pressure (see Appendix B)

$$\rho_{\mathrm{u}} v_{\mathrm{un}}^2 \approx \frac{p_{\mathrm{d}} + \frac{B_{\mathrm{dt}}^2}{2\mu_{\mathrm{o}}} - \frac{B_{\mathrm{ut}}^2}{2\mu_{\mathrm{o}}}}{\left(1 - \frac{B_{\mathrm{ut}}}{B_{\mathrm{dt}}}\right)} + \frac{B_{\mathrm{n}}^2}{\mu_{\mathrm{o}}} \approx \rho_{\mathrm{sw}} v_{\mathrm{sw}}^2 (\hat{\boldsymbol{v}}_{\mathrm{sw}} \cdot \hat{\boldsymbol{n}})^2, \tag{10}$$

where $\hat{\boldsymbol{v}}_{\mathrm{sw}}$ is the dimensionless unit vector corresponding to the solar wind flow direction, here taken to be radially outward from the Sun. The upstream Mach number can then be calculated from

$$M_{\mathrm{A}}^2 = \frac{\rho_{\mathrm{sw}} v_{\mathrm{sw}}^2}{\frac{|B_{\mathrm{u}}|^2}{\mu_{\mathrm{o}}}}. \tag{11}$$

[28] From equation 11, we see that M_{A} can be calculated without knowledge of the upstream solar wind speed or density. When solar wind speed estimates are available from FIPS as described in section 2.2, they can be used with equation 10 to estimate the upstream solar wind density. Motion of the BS will result in errors in the calculation of M_{A}. As will be discussed, however, we will apply this methodology only to orbits that show no evidence for multiple distinct bow shock crossings.

3. Plasma Depletion at Mercury

[29] The MESSENGER spacecraft is in a high-inclination, highly eccentric orbit around Mercury. As the planet orbits the Sun, the longitude of periapsis of the spacecraft moves through all local times with a period of 88 days, e.g., one Mercury year. Orbits with periapsis near local noon, as shown in Figure 4, have been termed "hot-season" orbits because of the increased temperatures experienced by the spacecraft when the low-altitude portion of the orbit is over the dayside hemisphere. These seasons occur when Mercury is at heliocentric distances of $R \sim 0.4$ AU. During these hot-season orbits, the spacecraft transits the MSH at low latitudes near the Sun-Mercury line, where the plasma is expected to be nearly stagnant. The spacecraft also passes through the magnetosheath southern flank near the orbital apoapsis. These regions are ideally suited for the application of the plasma parameter recoveries discussed in section 2, and therefore our analysis of magnetosheath plasmas is limited to only these types of orbits. The orbital period of MESSENGER around Mercury was 12 h during the spacecraft's primary mission (18 March 2011 – 16 March 2012) and was lowered to 8 h in mid-April 2012 for the probe's first extended mission [*McAdams et al.*, 2012]. The data used here come from four sets of hot-season orbits: 17– 29 November 2011, 10– 27 February 2012, and 29 July – 12 August 2012.

[30] The coordinate system used here is the Mercury solar magnetospheric (MSM) system [*Anderson et al.*, 2011], in which the X axis is directed from the center of the internal field dipole (offset ~0.2 R_{M} north of the planet's center, where R_{M} is Mercury's mean radius, 2440 km) to the Sun, the Z axis is directed northward along the planet's rotational axis, and the Y axis completes the right-handed coordinate system, as illustrated in Figure 4. As discussed in section 2, plasma density and temperature estimates are obtained in the subsolar region downstream of the bow shock and inside the magnetosphere. Plasma velocity and temperature estimates can be obtained in the solar wind and inside the flanks of the magnetosheath, under favorable spacecraft orientation [*Gershman et al.*, 2012].

3.1. Orbit Selection and Data Accumulation

[31] Although the subsolar magnetosheath transits studied here take place over only a few minutes, Mercury's magnetosphere and magnetosheath exhibit a wide range of dynamics as evidenced by multiple BS and MP boundary crossings and MP flux transfer events. To study the PDL, however, stable conditions through a given MSH transit are required. Thus, in addition to limiting our analysis to hot-season orbits favorable for FIPS analysis, we also limit events to those with: (1) no distinct multiple complete BS or MP crossings that last several tens of seconds, i.e., several multiples of the FIPS scanning periods of 10 s; (2) no clear discontinuities or sector crossings evident in either the plasma or magnetic field data in the MSH; (3) no strong peaks in the E/q plasma spectra from FIPS that would indicate possible fast downstream flows or dynamics; and (4) approximate pressure balance between the MSH and MP (i.e., within 30%). Guided by these criteria, we identified 40 orbits that are suitable for analysis. Boundary crossings were identified following the procedure described by *Winslow et al.* [2013]. The MSH data were taken between the outermost (with respect to the planet)

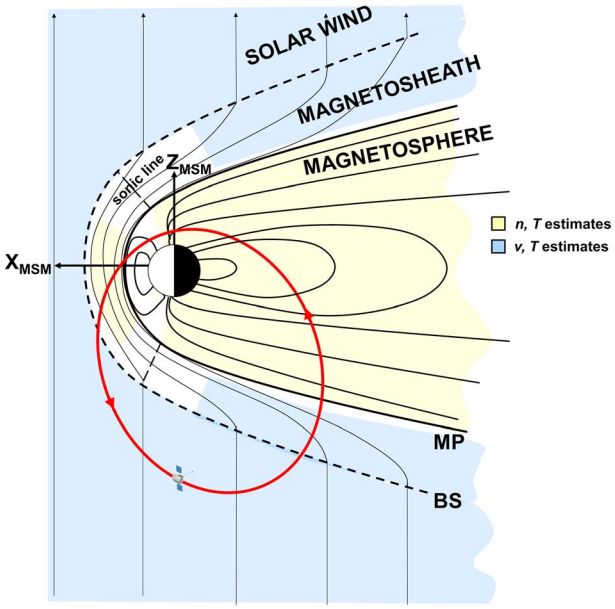

Figure 4. Illustration of Mercury's magnetosphere in the MSM *X-Z* plane. A typical MESSENGER spacecraft orbit trajectory during a hot-season orbit is shown (red). The spacecraft passes through the MSH in both the subsolar region and the southern flank. Plasma density and temperature are most reliably estimated in the subsolar MSH and in the nightside magnetosphere. Plasma velocity and temperature are most reliably estimated in the solar wind and magnetosheath flank.

partial MP crossing and the innermost partial BS crossing. These selection criteria naturally favor quasi-perpendicular bow shock geometry because of the difficulties associated with the determination of precise boundary locations for quasi-parallel bow shocks.

[32] Pressure balance at the MP was examined by comparing 1 min averages of $B^2/2\mu_o$ inside the MS with 1 min averages of $B^2/2\mu_o + 1.1 n_p k_B T_p$ inside the MSH. (Recall that the factor of 1.1 corresponds to the approximate thermal pressure contribution of He^{2+}). Because of relative motions of the MP boundary and the spacecraft, the transition from MS to MSH can exhibit multiple partial MP crossings. Hence, the calculations of MS and MSH pressures from MESSENGER data may correspond to different radial distances from Mercury. To compensate for this effect, we scale the $B^2/2\mu_o$ value from the MS by the expected radial variation of a dipole field [*Holzer and Slavin*, 1978], i.e., $1/R^3_{MSM.}$ It is this scaled pressure that is compared with the measured plasma thermal pressure.

[33] A number of metrics have been used to quantify plasma depletion. Early modeling work [*Lees*, 1964; *Zwan and Wolf*, 1976; *Siscoe et al.*, 2002] focused on the "depletion factor," the ratio of plasma density near the BS to that near the MP. *Farrugia et al.* [1995] and *Anderson et al.* [1997] used the change in plasma β, arguing that it represented both the reduction in plasma pressure and the increase in magnetic pressure associated with depletion. *Wang et al.* [2004] used the quantity n/B, in an attempt to capture the depletion of plasma and the increase of flux tube area. For our analysis, we define the "depletion ratio" to be the ratio of plasma β near the MP to that near the BS. Because observations of magnetic field magnitude are more precise and of higher cadence than the plasma data, we believe that using observed plasma β provides the most sensitive measurement of plasma depletion. As *Wang et al.* [2004] pointed out, using $\beta = 1$ to define the thickness of a depletion layer can be misleading because in low M_A environments the entire MSH can have $\beta < 1$. To avoid this problem, we identify the depletion layer as the region outward from the MP over which the calculated plasma β is less than $1/\sqrt{2}$ of β near the BS. The PDL thickness, D, is the difference in radial distance (in MSM) from the MP to this point.

[34] Because there is no upstream monitor at Mercury, any analysis of magnetospheric processes must rely on observations from only a single spacecraft. We are therefore limited in our ability to distinguish between variations in plasma parameters due to MSH processes and those of solar wind origin. To mitigate this issue, the orbits selected for our analysis are those that exhibited the least variation during an MSH transit. In addition, we tracked the variability of each plasma or magnetic field parameter calculated for each orbit. For example, for orbit-averaged plasma β values, we used 1 min averages of FIPS and MAG data close to the MP and BS boundaries. A 1 min average of plasma data includes ~5 FIPS E/q scans, and a 1 min average of magnetic field data includes ~1200 MAG data points. To compute such averages, we took the mean and standard deviation of all data points to compute the orbit-averaged value and variability, respectively. This variability was added in quadrature to any plasma parameter recovery uncertainty that was determined for an individual FIPS scan to provide the most quantitative metric for plasma depletion possible given the limitations of the available data sets.

[35] Temperatures on the order of ~1–5 MK will produce proton thermal speeds of ~100–200 km/s. Even with up to a factor of ~4 reduction in bulk speed across Mercury's bow shock and subsequent decrease towards the MP in the subsolar MSH, flow speeds of 50–100 km/s may be present, i.e., $v_o/v_{th} \sim 0.5$. As discussed in section 2.1, such flows can still result in reasonable density and temperature measurements for cases in which the flow direction is nearly perpendicular to the FIPS boresight direction. Here, we model the flow direction in the subsolar MSH as: $\hat{\boldsymbol{v}} = \hat{\boldsymbol{r}}_{MSM} \times (\hat{\boldsymbol{r}}_{MSM} \times \hat{\boldsymbol{x}}_{MSM})$, i.e., a flow directed away from the subsolar point and tangential to an assumed spherical boundary. Here, $\hat{\boldsymbol{r}}_{MSM}$ is the unit vector of the spacecraft position vector in MSM and $\hat{\boldsymbol{x}}_{MSM}$ is the unit vector corresponding to the X_{MSM} direction. With a known $\hat{\boldsymbol{v}}$, we can estimate $\theta_{v,FIPS}$, the angle between the flow direction and the FIPS boresight vector. The error estimates in $\theta_{v,FIPS}$ from Appendix A for $v_o/v_{th} = 0.5$ provide uncertainties in our recovered plasma parameters due to finite flow speed. These uncertainties are added in quadrature to those derived from counting statistics from section 2.1. In the subsolar MSH, the attitude of the MESSENGER spacecraft often produces $\theta_{v,FIPS} \sim 90°$, resulting in estimates of density and temperature throughout the MSH with predicted errors of < 20%.

3.2. Data Analysis

[36] Two example MESSENGER transits through the subsolar MSH are shown in Figure 5. On one orbit there was a prominent PDL under the condition of a quasi-perpendicular bow shock and northward IMF (Figure 5a), and on the second there was no evident PDL for an oblique bow shock geometry

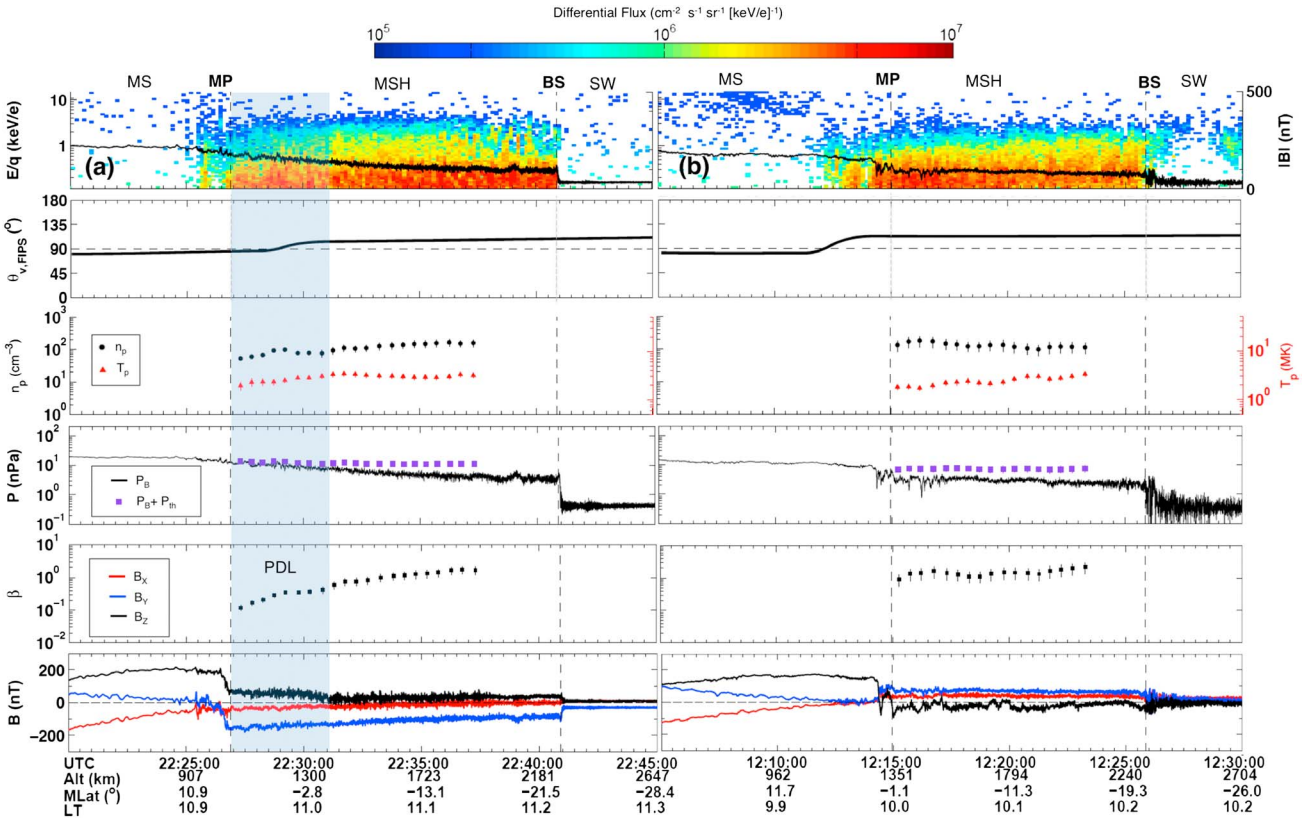

Figure 5. Example MESSENGER transits through the subsolar MSH under (a) quasi-perpendicular shock ($\theta_{BN} \approx 70°$) with upstream $M_A \sim 4$ from 23 November 2011, and (b) oblique shock ($\theta_{BN} \approx 45°$) with upstream $M_A \sim 3$ from 22 February 2012. For each, FIPS plasma and magnetic field parameters are shown. The angle between the modeled flow velocity and the FIPS boresight vector, $\theta_{v,FIPS}$, is shown in the second panel of both events; see Figure 2 for detailed descriptions of other plot panels. Uncertainties in all plasma parameters include both statistical counting errors and errors associated with a flow modeled with the scan-averaged $\theta_{v,FIPS}$ value and $v_o/v_{th} = 0.5$; a large-scale flux pileup and plasma depletion region has formed for the quasi-perpendicular case and is indicated by the shaded region. A smaller PDL region is shown for the quasi-parallel case.

and southward IMF (Figure 5b). For both examples $\theta_{v,FIPS} \sim 90°$ throughout the entire MSH transit, resulting in good estimates of plasma parameters. The quasi-perpendicular case ($\theta_{BN} \sim 70°$) with a PDL (Figure 5a) displayed a decreasing plasma pressure in tandem with an increasing B spread in space over a large fraction of the MSH. The resulting minimum depletion ratio, the ratio of β just outside the MP to that nearest to the BS, β_{MP}/β_{BS}, was ~0.1. The calculated solar wind dynamic pressure of ~15 nPa and upstream magnetic field magnitude of ~30 nT correspond to an upstream M_A of ~4. For this orbit, the solar wind speed was determined to be ~325 km/s, corresponding to a ~85 cm^{-3} solar wind density. The recovered plasma density just downstream of the BS is ~165 cm^{-3}, indicating a factor of ~2 density increase across the BS. In the MSH, $B_X \sim 0$, consistent with magnetic field draping in the subsolar region. In addition, there is no observable jump in B at the MP. The total pressure (magnetic plus thermal) is approximately constant, consistent with extended pressure balance layer that forms due to a largely sub-Alfvénic MSH environment in which the flow velocity was low and tangent to the magnetopause.

[37] The oblique ($\theta_{BN} \sim 45°$) shock case (Figure 5b) shows a nearly constant plasma density of ~120 cm^{-3} throughout the magnetosheath from the BS to the MP. A calculated solar wind dynamic pressure of ~11 nPa and upstream magnetic field magnitude of ~35 nT correspond to an upstream $M_A \sim 3$. For this orbit the solar wind speed was ~325 km/s, giving a solar wind density of ~60 cm^{-3} and a density compression factor of ~2 across the BS. There is a small signature of magnetic flux pileup with an increase in B between the BS and MP. However, the magnetic field inside the MSH has a substantial positive B_X, indicating that it is not well draped around the subsolar magnetopause, a geometry that inhibits plasma depletion. The calculated depletion ratio is ~0.7.

[38] These examples illustrate the expected behavior for a PDL in which strong depletion typically occurs for well-draped northward IMF (Figure 5a) whereas the combined effects of reconnection for southward IMF and a strong normal magnetic field at the shock inhibit PDL formation (Figure 5b). This clear distinction is not always evident at Mercury, however, as the more comprehensive statistical study presented below shows. The statistical study is based on the recovered plasma properties for the full set of selected orbits listed in Tables 1 and 2 for quasi-perpendicular and quasi-parallel shock geometry, respectively.

Table 1. MESSENGER Plasma and Magnetic Field Observations Near Quasi-Parallel ($\theta_{BN} < 45°$) Bow Shocks

Date	MSH Start (UTC)	MSH Stop (UTC)	<LT> (h)	θ_{BN} (°)	$\lvert\mathbf{B}\rvert_{IMF}$ (nT)	$\lvert\mathbf{B}\rvert_{BS}$ (nT)	n_{BS} (cm^{-3})	T_{BS} (MK)	β_{BS}	β_{MP}	θ_D (°)	θ_S (°)	D (km)
18 Nov 2011	22:31:00	22:43:19	12.7	29 ±12	37.5 ±6.0	53.0 ±10.3	48 ±20	2.3 ±0.6	1.15 ±0.47	0.59 ±0.30	102 ±19	38 ±19	101 ±0
21 Nov 2011	22:33:36	22:46:19	11.9	43 ±17	29.6 ±4.8	56.9 ±6.4	223 ±79	1.2 ±0.3	2.80 ±0.93	1.73 ±0.31	79 ±7	76 ±7	126 ±59
29 Nov 2011	10:30:50	10:36:17	9.1	39 ±18	13.0 ±3.9	36.3 ±9.8	181 ±93	3.1 ±0.4	18.15 ±10.71	3.60 ±2.46	88 ±9	55 ±9	181 ±0
13 Feb 2012	04:16:49	04:26:48	13.1	39 ±16	20.7 ±4.2	52.2 ±15.2	342 ±158	1.8 ±0.6	15.64 ±8.77	3.13 ±2.07	81 ±19	93 ±19	278 ±177
18 Feb 2012	02:06:42	02:17:16	11.6	34 ±16	29.3 ±5.7	70.2 ±9.2	109 ±17	4.0 ±0.3	2.28 ±0.41	0.17 ±0.15	88 ±7	103 ±7	664 ±67
17 Aug 2012	07:45:05	07:56:42	9.6	31 ±15	37.1 ±7.3	85.5 ±11.9	73 ±30	7.0 ±1.0	2.03 ±0.84	0.19 ±0.07	89 ±10	150 ±10	373 ±0
18 Aug 2012	23:46:14	23:57:35	9.0	41 ±17	41.6 ±10.9	106.3 ±10.9	168 ±80	4.0 ±0.3	2.34 ±1.09	0.25 ±0.09	81 ±8	92 ±8	331 ±9

Note: The uncertainties for each value include the variability over the averaging time interval and the estimated plasma parameter recovery errors added in quadrature.

[39] For each orbit, we calculated plasma parameters for each FIPS scan in the MSH from the MP outward toward the BS along 75% of the MSH transit, as discussed in section 2. Near the BS and MP boundaries, plasma parameters were calculated from 1 min averages of parameters recovered closest to each boundary. The draping angle [*Coleman et al.*, 2000; *Coleman*, 2005], θ_D, is the angle between the MSH magnetic field and the average MP normal vector from *Winslow et al.* [2013] and is 90° for a well-draped field. The shear angle across the MP, θ_S, was calculated from the magnetic field direction averaged over 1 min inside the MP and the observed field direction throughout the MSH. As discussed in section 3.1, the variability of all parameters over the time-average interval was also calculated. The shock angle, θ_{BN}, and upstream M_A values were calculated with the methods introduced in section 2.3. The variation in the IMF both in magnitude and orientation was used to determine the variability of θ_{BN} and M_A. The PDL thickness, D, was calculated following section 3.1 using two values of β_{BS}: the variability added to and subtracted from the mean value. For orbits in which the plasma β rises above $1/\sqrt{2}$ times the full range of β_{BS} values in a single FIPS E/q scan, there is no reported variation in the thickness.

3.2.1. IMF Orientation Effects on Plasma Depletion

[40] The depletion ratio is shown in Figure 6 as a function of shock angle, shear angle, and draping angle for all events under quasi-parallel ($\theta_{BN} < 45°$) (Table 1) and quasi-perpendicular ($\theta_{BN} > 45°$) (Table 2) conditions. Some amount of depletion is evident for nearly every event, regardless of shock geometry (Figure 6a). The strongest depletion occurs for well-draped fields, $\theta_D \sim 90°$, implying that even for the quasi-parallel shock cases at Mercury, the field drapes around the magnetosphere (Figure 6b). Depletion does not appear to be a strong function of magnetic shear angle at the MP, in that strong depletion occurs for both low and high magnetic shear (Figure 6c). For the data set considered here, although IMF orientation fluctuates, the events can still be classified into a low shear ($\theta_S < 90°$) or high shear ($\theta_S > 90°$) events.

3.2.2. Upstream M_A Effects on Plasma Depletion

[41] We examined the depletion ratio and PDL thickness as functions of upstream M_A for both low shear and high shear events. The results are shown in Figure 7, in which the depletion ratio and layer thickness are plotted versus upstream M_A. PDL thickness is shown only for those events with depletion ratios below $1/\sqrt{2}$, consistent with our definition of the outer edge of the PDL. The predicted thickness from *Zwan and Wolf* [1976], i.e., $D \approx 1.24 R_{MP}/M_A^2$, where R_{MP} is the standoff distance of the subsolar magnetopause, is also shown. Although we rely on a different definition of D, we expect the thinnest and least depleted PDLs for high M_A during high shear, and the thickest and most depleted PDLs for low M_A during low shear. However, there are examples of high shear and low shear events that show strong and weak depletion for both low and high M_A.

[42] An example of a thin PDL formed under a low M_A (~4) and low shear (θ_S ~60°) is shown in Figure 8. The upstream plasma conditions are similar to those of the quasi-perpendicular example shown in Figure 5a, but no substantial flux pileup or plasma depletion is observed. The upstream IMF for this orbit has a large positive B_Z, and near the MP we also see evidence of a positive B_X. At Earth, we would expect that the combination of a

Table 2. MESSENGER Plasma and Magnetic Field Observations Near Quasi-Perpendicular ($\theta_{BN} \geq 45°$) Bow Shocks

Date	MSH Start (UTC)	MSH Stop (UTC)	<LT> (h)	θ_{BN} (°)	$\lvert\mathbf{B}\rvert_{IMF}$ (nT)	$\lvert\mathbf{B}\rvert_{BS}$ (nT)	n_{BS} (cm^{-3})	T_{BS} (MK)	β_{BS}	β_{MP}	θ_D (°)	θ_S (°)	D (km)
11 Nov 2011	22:30:49	22:39:00	14.6	51 ±22	12.3 ±4.4	33.0 ±10.9	183 ±69	1.4 ±0.3	6.00 ±2.53	3.94 ±2.23	91 ±10	150 ±10	76 ±8
18 Nov 2011	10:27:48	10:51:41	12.9	52 ±5	44.2 ±4.1	93.2 ±3.9	59 ±21	1.9 ±0.3	0.39 ±0.15	0.03 ±0.01	87 ±5	122 ±5	291 ±9
21 Nov 2011	10:30:50	10:50:50	12.0	83 ±3	26.2 ±1.4	67.0 ±4.7	53 ±19	2.0 ±0.3	0.83 ±0.33	0.12 ±0.04	80 ±6	50 ±6	478 ±26
22 Nov 2011	10:34:25	10:45:53	11.7	62 ±12	26.0 ±3.1	49. ± 10.4	254 ±68	1.2 ±0.2	3.02 ±0.88	0.93 ±0.20	79 ±12	87 ±12	183 ±0
23 Nov 2011	22:26:53	22:40:54	11.1	73 ±6	33.0 ±3.0	93.8 ±7.3	164 ±40	3.1 ±0.6	1.89 ±0.63	0.16 ±0.04	84 ±6	74 ±6	739 ±83
11 Feb 2012	05:08:11	05:17:55	13.6	64 ±11	14.1 ±2.8	42.5 ±12.4	172 ±52	3.1 ±0.6	20.87 ±12.45	3.79 ±1.65	85 ±12	54 ±12	339 ±204
11 Feb 2012	16:56:42	17:07:17	13.5	68 ±17	24.6 ±7.0	45.9 ±7.9	199 ±86	2.3 ±0.5	6.30 ±2.40	1.58 ±0.55	85 ±7	67 ±7	366 ±60
12 Feb 2012	04:43:30	04:56:52	13.4	52 ±23	15.2 ±3.5	52.0 ±8.2	71 ±27	3.7 ±0.8	2.89 ±1.17	0.42 ±0.32	83 ±7	78 ±7	662 ±169
17 Feb 2012	14:20:12	14:32:14	11.8	55 ±20	35.5 ±11.1	80.0 ±12.3	95 ±10	4.6 ±0.3	2.25 ±0.29	0.32 ±0.13	89 ±6	111 ±6	667 ±0
19 Feb 2012	01:40:24	01:52:35	11.3	52 ±12	27.2 ±3.6	77.2 ±16.4	94 ±27	5.2 ±1.0	2.51 ±0.80	0.50 ±0.39	93 ±10	145 ±10	735 ±25
19 Feb 2012	13:29:25	13:41:45	11.1	53 ±20	31.6 ±7.9	72.3 ±7.8	110 ±28	4.2 ±0.6	3.00 ±0.96	0.24 ±0.10	87 ±8	113 ±8	549 ±34
20 Feb 2012	01:19:05	01:26:41	11.0	45 ±17	30.2 ±7.9	70.0 ±8.4	194 ±62	2.2 ±0.3	2.81 ±0.97	1.14 ±0.38	78 ±6	51 ±6	216 ±33
20 Feb 2012	13:04:21	13:17:28	10.8	73 ±12	27.6 ±5.4	84.1 ±8.9	105 ±40	4.7 ±0.8	2.94 ±1.08	0.42 ±0.13	88 ±5	98 ±5	765 ±84
21 Feb 2012	12:38:39	12:52:50	10.5	54 ±17	34.7 ±7.1	78.0 ±8.1	143 ±53	3.4 ±0.6	2.76 ±1.14	0.91 ±0.35	77 ±6	67 ±6	405 ±126
22 Feb 2012	12:14:57	12:25:52	10.1	47 ±19	34.5 ±8.6	75.0 ±7.5	119 ±49	3.0 ±0.6	2.17 ±0.87	1.55 ±0.79	82 ±4	105 ±4	82 ±0
24 Feb 2012	23:08:38	23:15:51	9.1	49 ±18	34.0 ±7.1	88.9 ±14.7	346 ±164	2.8 ±0.4	5.31 ±3.22	1.92 ±0.99	80 ±8	66 ±8	121 ±24
26 Feb 2012	10:28:09	10:40:54	8.5	70 ±10	28.9 ±3.6	87.4 ±12.9	205 ±97	3.0 ±0.4	3.16 ±1.56	2.49 ±1.25	78 ±10	64 ±10	31 ±0
4 May 2012	07:33:22	07:56:10	14.9	81 ±7	25.7 ±3.9	64.2 ±6.8	21 ±12	2.6 ±1.0	0.48 ±0.25	0.18 ±0.10	102 ±6	142 ±6	197 ±89
7 May 2012	15:32:22	15:49:24	14.1	69 ±12	23.1 ±3.9	60.0 ±8.3	106 ±41	1.4 ±0.2	1.46 ±0.65	0.08 ±0.04	85 ±4	60 ±4	989 ±85
14 May 2012	07:27:12	07:36:46	12.1	50 ±18	29.5 ±7.3	85.3 ±16.2	117 ±29	8.4 ±1.6	3.62 ±0.72	0.68 ±0.26	93 ±8	165 ±8	415 ±45
30 Jul 2012	15:45:12	15:59:59	14.8	80 ±9	34.6 ±6.2	84.8 ±13.2	60 ±25	5.8 ±1.4	1.60 ±0.70	0.35 ±0.14	97 ±7	89 ±7	481 ±132
2 Aug 2012	23:44:53	23:58:16	14.0	51 ±19	23.1 ±4.9	62.3 ±8.0	10 ±10	5.6 ±2.5	0.42 ±0.25	0.10 ±0.06	90 ±7	41 ±7	234 ±131
3 Aug 2012	15:49:54	16:04:56	13.9	87 ±2	18.1 ±1.7	46.1 ±8.6	29 ±13	4.6 ±1.0	1.91 ±1.06	0.41 ±0.25	101 ±9	143 ±9	487 ±155
4 Aug 2012	15:46:25	15:59:43	13.6	72 ±7	18.7 ±3.6	55.6 ±8.7	87 ±31	2.2 ±0.5	2.08 ±0.82	0.63 ±0.33	98 ±7	147 ±7	201 ±167
5 Aug 2012	15:46:29	15:57:15	13.4	55 ±18	15.8 ±3.9	45.7 ±8.0	163 ±50	2.5 ±0.5	9.40 ±3.43	4.34 ±2.39	95 ±10	114 ±10	140 ±88
5 Aug 2012	23:43:28	23:54:36	13.2	78 ±5	20.4 ±1.4	74.1 ±17.4	167 ±22	3.9 ±0.5	4.37 ±0.98	1.36 ±0.42	92 ±8	114 ±8	459 ±183
7 Aug 2012	07:46:56	07:57:00	12.9	85 ±4	21.3 ±3.7	66.0 ±11.2	49 ±9	4.1 ±0.9	1.09 ±0.22	0.48 ±0.13	96 ±8	122 ±8	225 ±17
8 Aug 2012	07:43:48	07:58:37	12.6	57 ±10	38.8 ±4.5	101.1 ±10.6	56 ±10	4.9 ±0.9	0.71 ±0.15	0.18 ±0.13	88 ±5	103 ±5	449 ±122
9 Aug 2012	15:42:25	15:51:38	12.1	58 ±10	36.5 ±4.0	117.0 ±13.9	81 ±27	2.5 ±0.4	0.32 ±0.11	0.38 ±0.08	91 ±3	67 ±3	32 ±0
10 Aug 2012	07:45:33	07:57:20	12.0	67 ±15	23.8 ±6.5	66.6 ±9.1	39 ±7	5.0 ±1.0	1.24 ±0.40	0.14 ±0.15	80 ±8	37 ±8	599 ±131
11 Aug 2012	07:42:52	07:53:58	11.7	61 ±22	44.5 ±11.9	101.9 ±15.3	68 ±7	6.0 ±0.9	1.47 ±0.28	0.20 ±0.08	81 ±9	46 ±9	560 ±52
13 Aug 2012	07:48:21	08:04:46	11.1	62 ±12	35.7 ±6.9	83.9 ±8.4	54 ±15	2.6 ±0.4	0.67 ±0.20	0.10 ±0.05	76 ±10	64 ±10	634 ±60
16 Aug 2012	07:46:28	08:00:29	10.0	58 ±17	42.1 ±9.9	85.8 ±8.8	72 ±37	2.7 ±0.5	0.72 ±0.43	0.29 ±0.11	79 ±7	62 ±7	275 ±224

Note: The uncertainties for each value include the variability over the averaging time interval and the estimated plasma parameter recovery errors added in quadrature.

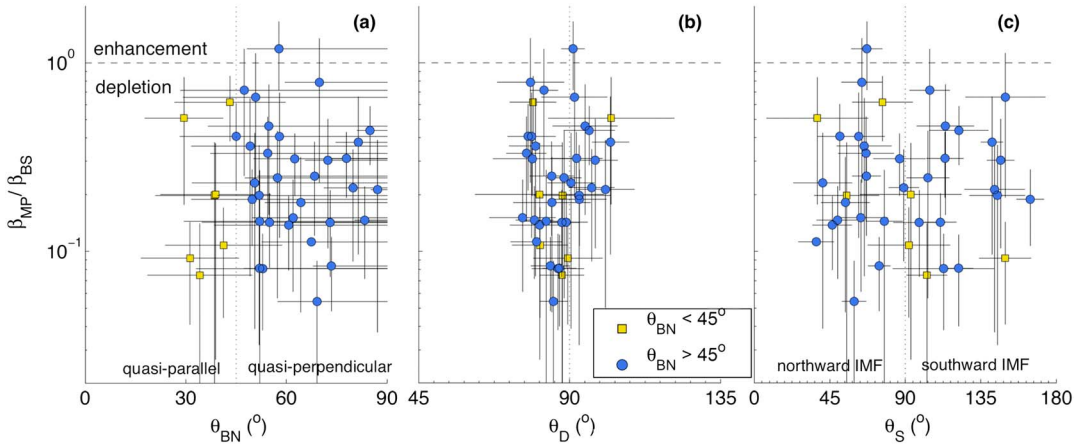

Figure 6. Measured plasma depletion, $\beta_{MP}/\beta_{BS,}$ as a function of (a) shock angle (θ_{RN}), (b) magnetopause draping angle (θ_D), and (c) magnetopause shear angle (θ_S). Events are separated into groups of quasi-parallel (yellow squares) and quasi-perpendicular (blue circles) shocks. Some amount of plasma depletion is observed under all upstream conditions.

northward, anti-sunward magnetic field and a low upstream M_A would maximize reconnection in the magnetic cusp [*Le et al*., 1994, 1996; *Onsager et al*., 2001; *Winslow et al*., 2012]. For cusp reconnection, if multiple merging sites form between the MS lobe field lines and draped MSH field, such a situation will result in the formation of flux ropes that move away from the subsolar region in the east-west direction, in contrast to the north-south direction of motion associated with subsolar reconnection processes [*Berchem et al*., 1995]. The net effect of these reconnection processes, however, is the same: substantial amounts of magnetic flux are removed from the dayside. At Earth, both PDLs [*Anderson et al*., 1997] and cusp reconnection [*Phan et al*., 2003] are nearly always observed for northward IMF, implying that cusp reconnection may not be of dynamic importance for PDL formation. However, the dominant mechanisms of magnetic flux transport at Mercury are still under investigation. Our observations may imply that cusp reconnection at Mercury and the resulting FTE showers [*Slavin et al*., 2012] transport greater relative amounts of flux than at Earth, resulting in inhibited large-scale PDL formation at the low-shear MP.

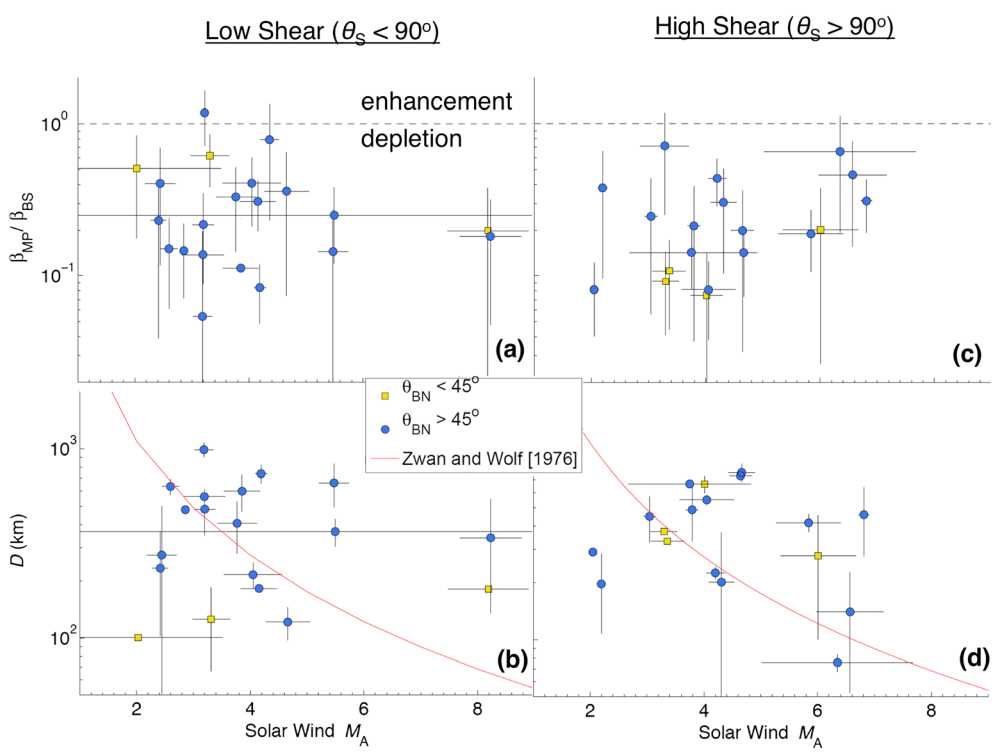

Figure 7. (a) Measured plasma depletion, $\beta_{MP}/\beta_{BS,}$ and (b) measured PDL thickness, D, as a function of upstream M_A for events with low shear (θ_S <90°). Figures 7c and 7d are identical to Figures 7a and 7b, respectively, but for events with high shear (θ_S >90°).

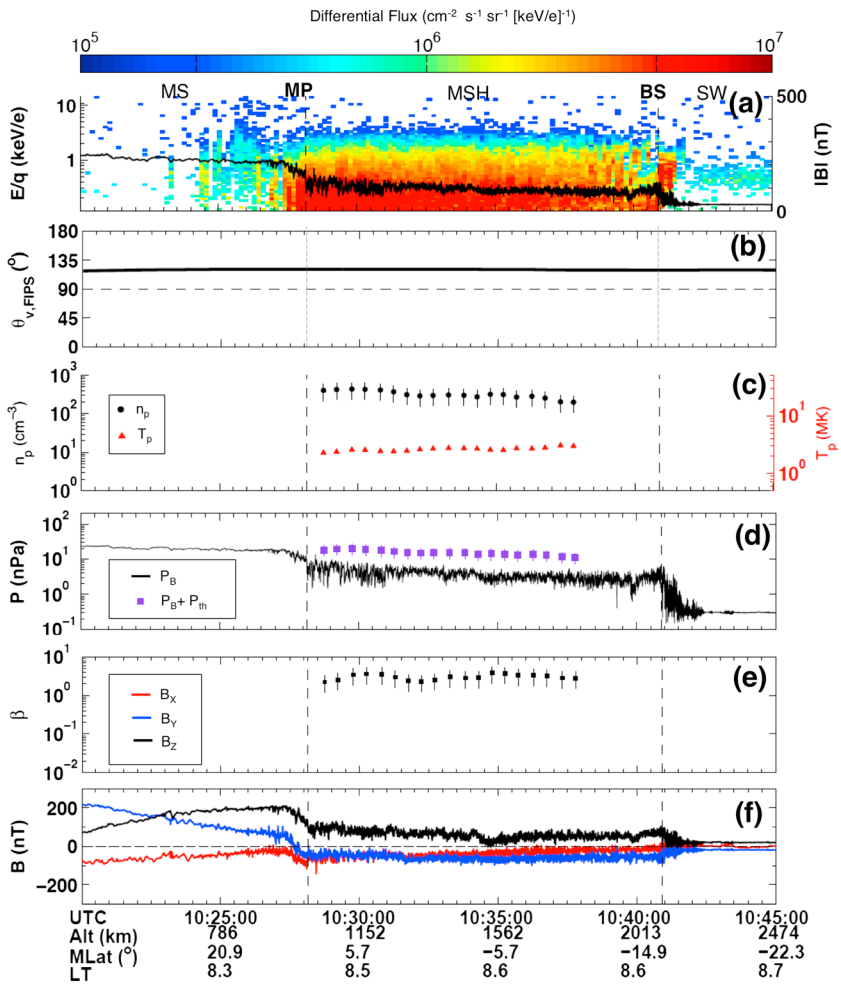

Figure 8. Same as Figure 5 but for an example orbit with upstream $M_A \sim 4$ and low shear ($\theta_S \sim 60°$) on 26 February 2012. This example is marked by inhibited plasma depletion for northward IMF and low M_A.

3.2.3. Time and Length Scales of Plasma Depletion

[43] Because flow speeds in the MSH should scale with the upstream solar wind speed, [*Spreiter et al.*, 1966; *Siscoe et al.*, 2002] we expect that, to first order, the time for plasma to flow around a planetary obstacle scales as

$$\tau_{dep} \propto \frac{R_{MP}}{v_{sw}}. \tag{12}$$

[44] At first glance, this timescale may appear to be in direct contradiction with the predictions of *Zwan and Wolf*

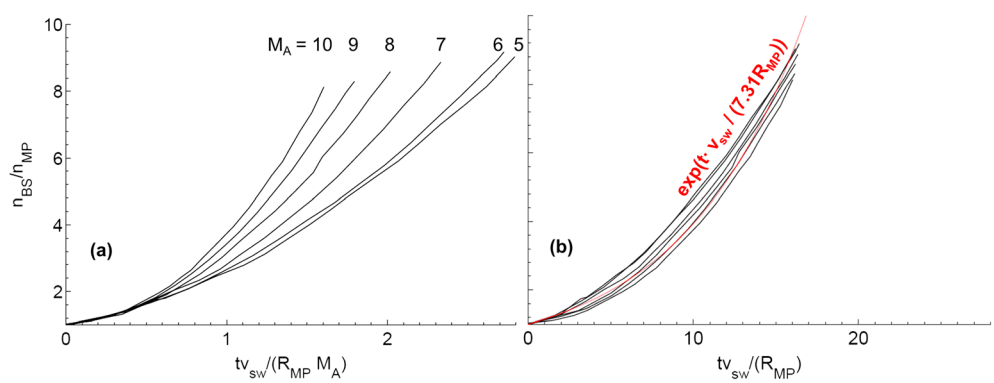

Figure 9. (a) Density depletion factor (n_{BS}/n_{MP}) as a function of scaled time, $t\ v_{sw}/(R_{MP}\ M_A)$, digitized from Figure 8 in *Zwan and Wolf* [1976]. (b) Depletion factor with a rescaled time of $t\ v_{sw}/(R_{MP})$. A best fit exponential curve, shown in red, is used to estimate the average timescale for particle escape from the subsolar region.

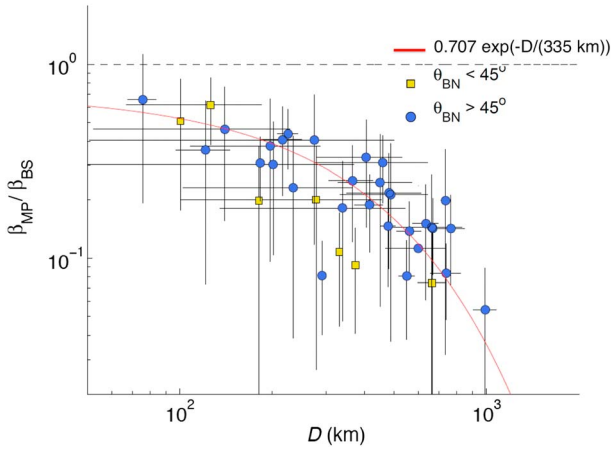

Figure 10. Depletion ratio β_{MP}/β_{BS} as a function of measured PDL thickness, D, for all orbits with $\beta_{MP}/\beta_{BS} < 1/\sqrt{2}$, regardless of upstream conditions. Events from quasi-parallel and quasi-perpendicular shocks are shown as yellow squares and blue circles, respectively. A best fit exponential relationship of the form of equation 15 (red line) is shown to match the data well, indicating that there is a characteristic length scale of depletion of 335 ± 49 km at Mercury, equivalent to ~0.1 R_{MP}.

[1976], by which the timescale of plasma depletion is a function of M_A. This variation is shown in Figure 9a, a plot of the depletion factor from *Zwan and Wolf* [1976] as a function of their dimensionless time variable, $t\, v_{sw}/(R_{MP}\, M_A)$. However, when this quantity is rescaled to form $t\, v_{sw}/(R_{MP})$ as shown in Figure 9b, much of this variability is removed, indicating that the M_A dependence of the depletion timescale is secondary to the upstream solar wind speed and the size of the planetary obstacle. From these rescaled values, we calculate an approximate depletion timescale of,

$$\tau_{dep} \approx 7.31 \frac{R_{MP}}{v_{sw}}\,\mathrm{s}, \tag{13}$$

where R_{MP} is in units of km and v_{sw} is in units of km/s. For $v_{sw} = 400$ km/s we calculate depletion timescales of ~1 min and ~20 min for Mercury ($R_{MP} = 1.45\ R_M$ [*Winslow et al.*, 2013]) and Earth ($R_{MP} = 11 R_E$, where R_E is the Earth's radius [*Fairfield*, 1979]), respectively.

[45] We can compare this depletion time with residence time for a flux tube within a distance D_{dep} of the magnetopause. Again, because the flow in the magnetosheath scales with v_{sw}, we expect

$$\tau_{res} \propto \frac{D_{dep}}{v_{sw}} \tag{14}$$

[46] We require $\tau_{res} \sim \tau_{dep}$ for a depletion layer to form, resulting in $D_{dep} \propto R_{MP}$. Here, D_{dep} is a characteristic distance over which plasma can deplete at a planetary body. Its precise value, in general, will depend on the particular measure of depletion used. Here, we use

$$\frac{\beta_{MP}}{\beta_{BS}} \approx \frac{1}{\sqrt{2}} \exp\left(-D/D_{dep}\right) \tag{15}$$

where the factor of $1/\sqrt{2}$ arises from our definition of D.

[47] As discussed above, the upstream conditions, namely M_A and IMF orientation, determine the range of depletion and thicknesses possible at a planetary body. However, here we see that the relationship between the amount of depletion that occurs for a particular layer thickness is to lowest order a function only of obstacle geometry. The value of such a relationship is that it enables localized measurements of the β value at the MP and at the BS to describe the large-scale behavior of solar wind flow around a planetary body.

[48] To test the validity of this relationship at Mercury, we examine the relationship between the observed depletion, β_{MP}/β_{BS}, and the observed thickness D. Data from all orbits, with $\beta_{MP}/\beta_{BS} < 1/\sqrt{2}$, regardless of upstream conditions, are shown in Figure 10. We see that these data, on average, are well represented by a relation of the form of equation 15. To evaluate a best fit value of D_{dep} that takes into account the uncertainties in both β_{MP}/β_{BS} and D, we employed a bootstrap-like Monte Carlo analysis [*Hesterberg et al.*, 2010]. Each (D,β_{MP}/β_{BS}) point was resampled from a two-dimensional Gaussian distribution with mean and standard deviations corresponding to average value and uncertainties in their respective parameters. The value of D_{dep} that minimizes the mean squared error between the resampled points and a curve of the form of equation 15 was calculated. This process was repeated for 10,000 resamplings, resulting in a distribution of best fit D_{dep} values with mean and standard deviation of 335 km and 49 km, respectively, corresponding to $D_{dep} \sim 0.1\ R_{MP}$. By the nature of our definition of D, we cannot characterize a depletion layer over the entire MSH (~0.5 R_M). However, we can estimate a lower bound of ~0.005 for the depletion ratio at Mercury by substituting $D_{dep} = 0.1\ R_{MP}$ and $D = 0.5\ R_M$ in equation 15.

4. Discussion

[49] Our findings are consistent with the *Zwan and Wolf* [1976] prediction that the value of upstream M_A exerts an important control on the plasma depletion process. The lower the upstream M_A value, the larger the possible scale of flux pileup and plasma depletion in the MSH, and other factors such as shock geometry and IMF orientation serve to modulate the thickness of the PDL that ultimately forms. A lower average upstream M_A at Mercury than at Earth results in PDLs that can potentially occupy a larger fraction of the MSH. We also find examples of inhibited plasma depletion for low shear at the MP and for low M_A that appear to be a specific consequence of Mercury's magnetospheric environment.

[50] Minimum variance analysis of the magnetic field at Mercury's MP reveals that the MP reconnection rate at Mercury is nearly independent of shear angle [*DiBraccio et al.*, 2013]. The calculated MP reconnection rate at the magnetopause was further shown to increase for decreasing MP plasma β values, consistent with the view that plasmas with high Alfvén speeds transport large amounts of flux away from the subsolar region. The low β_{MP} formed as a consequence of PDL formation promotes substantial reconnection even for low shear angles. This reconnection, however, is not sufficient to transport all of the piled-up magnetic flux in the MSH around the magnetosphere; this flux overwhelms the MP reconnection process. This pileup results in large-scale, persistent PDLs that may produce prolonged increases in the average MP reconnection rate at Mercury.

Table 3. Summarized Observations of Plasma Depletion Throughout the Solar System

Location	Description	Obstacle Size (i.e., R_{MP})	β_{MP}/β_{BS}	Duration	D	D_{dep}
Mercury	This work	1.45 R_M	-	-	-	(0.08–0.11) R_M
Earth	Superposed epoch analysis of PDLs with low shear MP, Figure 9 from *Phan et al.* [1994]	11 R_E	0.25	7 min	(~0.15–0.65) R_E	(~0.15 – 0.65) R_E
Mars	Example #2, Figure 3 from *Øieroset et al.* [2004]	1.05 R_{MARS}	0.15	5 min	~0.15 R_{MARS}	~ 0.1 R_{MARS}
Jupiter	Figure 2 from *Joy et al.* [2006]	110 $R_{JUPITER}$	< 0.125	120–600 min	(~ 10 – 33) $R_{JUPITER}$	(~5–20) $R_{JUPITER}$
Saturn	Example #2, Figure 2 from *Violante et al.* [1995]	22 R_{SATURN}	0.12	150 min	~1.8 R_{SATURN}	~ 1.0 R_{SATURN}
ICME	Superposed epoch analysis of PDLs in magnetic cloud ICMES, Figure 8 from *Liu et al.* [2006a]	1 AU	0.5	180 min	~0.04 AU	~ 0.1 AU

[51] Observations at Earth show that plasma depletion leads to a regular evolution in temperature anisotropy, $A = T_\perp/T_\parallel - 1$, and corresponding plasma instabilities [*Denton et al.*, 1994]. The perpendicular flux tube compression increases $T_\perp$ and the parallel expansion decreases $T_\parallel$, creating a temperature anisotropy $A = 0.5$ to 4 [*Phan et al.*, 1994; *Fuselier et al.*, 1994; *Anderson et al.*, 1997]. This anisotropy drives electromagnetic ion cyclotron (EMIC) and mirror-mode waves, which reduce the anisotropy. The net result is a marginally stable system in which A and $\beta_\parallel$ fall along the threshold for the EMIC and mirror-mode instabilities; at the threshold, the anisotropy scales as $A \sim a \cdot \beta_\parallel^{-b}$ where $a \sim 1$, $b \sim 0.5$, and $\beta_\parallel = \mu_0 n k_B T_\parallel / B^2$ [*Gary et al.*, 1993; *Fuselier et al.*, 1994; *Gary et al.*, 1997]. The lower average plasma β in Mercury's MSH favors the generation of EMIC waves over mirror-mode waves because for $\beta_\parallel < 1$ the EMIC instability threshold is at lower anisotropy. Although measurements of temperature anisotropy are not available for the MESSENGER orbits studied here, fluctuations with $|\delta \mathbf{B}|/B \sim 1$ are present through much of Mercury's MSH with frequencies up to ~1 Hz, consistent with the expected range of observable Doppler-shifted proton cyclotron frequencies.

[52] We conclude that the observed plasma depletion processes at Mercury are analogous to those observed elsewhere in the solar system. Consequently, we expect that the length scale of plasma depletion found at Mercury, $D_{dep} \sim 0.1 R_{MP}$, applies to other planetary systems. To examine this assertion, we summarize observations made of plasma depletion in a variety of space environments in Table 3. For each, we have estimated the depletion ratio, β_{MP}/β_{BS}, and layer thickness D, and used equation 15 to calculate D_{dep}. For Earth, *Phan et al.* [1994] estimated an upper and lower bound for the layer thickness. For Mars, Jupiter, and Saturn, these distances were estimated from plots provided by *Øieroset et al.* [2004], *Joy et al.* [2006], and *Violante et al.* [1995], respectively. We also include interplanetary coronal mass ejection (ICME) events studied by *Liu et al.* [2006a]. For those events, the thickness was calculated from the product of the duration of the indicated PDL times and the bulk speed of the plasma, 500 km/s. Since the ICME events were observed at Earth during solar maximum, we assume a radius of curvature of ~ 1 AU [*Liu et al.*, 2006b]. Although extensive studies of magnetic pileup boundaries (MPBs) have been conducted at Venus [*Zhang et al.*, 1991; *Bertucci et al.*, 2003b, 2005], to our knowledge there are no published plasma and magnetic field data time series that enable a calculation of MSH β as a function of distance from the MPB. As shown in Figure 11, for all environments, the length scale of plasma depletion is closely related to the size of the magnetic obstacle, R_{MP}. A least squares solution to these data gives $D_{dep} = 0.100 \pm 0.002\ R_{MP}$, where the uncertainty here is the standard error. Such a scaling allows for the comparison of depletion processes at different planetary bodies despite the large range of upstream conditions found throughout the solar system.

5. Concluding Remarks

[53] We have analyzed 40 events in the subsolar MSH of Mercury for evidence of magnetic flux pileup and plasma depletion. Subsolar plasma depletion occurs at Mercury for nearly all upstream conditions, with the strongest depletion effects observed for low values of M_A. PDL formation is highly variable even for low M_A and northward IMF, possibly as a result of enhanced reconnection and flux rope formation near the cusp, though further investigation is required to determine the dynamic coupling, if any, between the two processes. In addition, it appears that plasma depletion plays a role in magnetic reconnection at Mercury because for the MSH environment of Mercury, large-scale PDLs overlie the MP boundary with low β plasma, creating an environment that promotes the frequent, high-rate MP reconnection

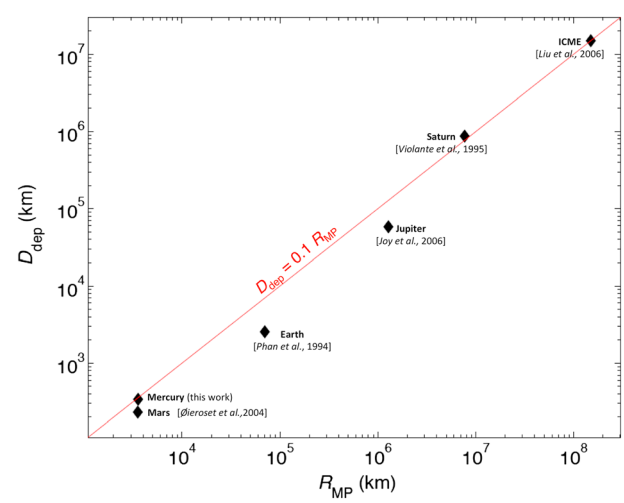

Figure 11. Derived depletion scale length (D_{dep}) from Table 3 as a function of obstacle size for PDLs measured throughout the solar system. A least squares solution to these data gives $D_{dep} = 0.100 \pm 0.002\ R_{MP}$. These data indicate that the length scale of depletion at a planetary body is most strongly set by its physical size, i.e., the process is self-similar at all systems.

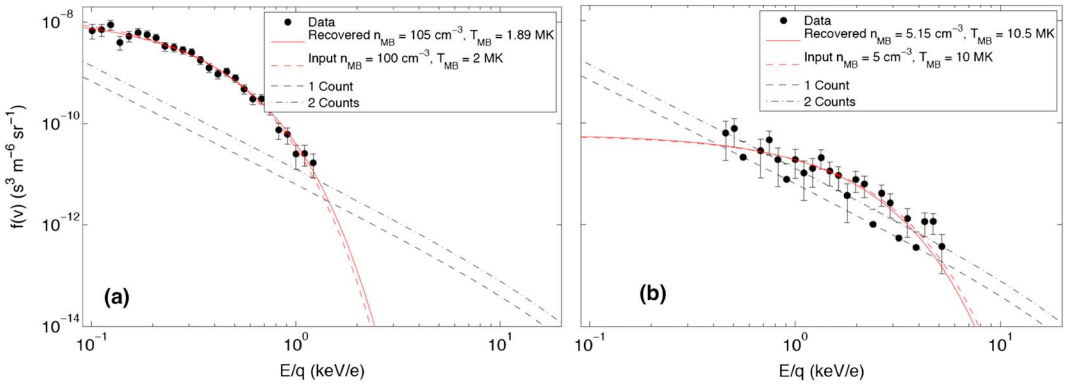

Figure A1. Phase space distributions for synthetic distributions with (a) $n = 100\,\mathrm{cm}^{-3}$, $T = 2$ MK and (b) $n = 5\,\mathrm{cm}^{-3}$, $T = 10$ MK. The true curve appears as a solid red line. Generated events (black circles) are processed and converted to phase space density. The phase space distribution corresponding to the density and temperature recovered from the synthetic events is shown as a dashed red curve. For hot, sparse distributions (i.e., the plasma sheet), particles with $v < v_{\min}$ will not generate an event within a given accumulation time of data.

reported by *Slavin et al*. [2009] and *DiBraccio et al*. [2013]. Finally, we find a characteristic depletion length scale of 335 ± 49 km at Mercury, equivalent to ~0.1 R_{MP}. This scale has been shown to apply to other planetary bodies throughout the solar system. These results illustrate the intrinsic value of studying Mercury's magnetosphere and its dynamics because the magnetospheric system of Mercury presents a regime of plasmas and shock conditions that are rarely observed elsewhere in the solar system. During the remainder of its mission, MESSENGER will continue to explore the distinctive plasmas and magnetic fields found in the inner solar system.

Appendix A: Plasma Density and Temperature Recovery Errors

[54] The recovery of density and temperature introduced in section 2.1 was tested with synthetic events using a forward model of the FIPS sensor. The phase space density from an input proton velocity distribution was sampled in the FIPS instrument frame with 2.5° angular resolution. Values of the zenith angle (θ_{FIPS}) between 15° and 75° from the FIPS boresight direction and azimuthal angle (ϕ_{FIPS}) between 0° and 360° were sampled, simulating ~1.4π sr of total visibility. At each angular bin and energy-per-charge step, the number of measured events, $N(E/q,\theta_{\mathrm{FIPS}},\phi_{\mathrm{FIPS}})$, was calculated from the phase space density distribution, $f(E/q,\theta_{\mathrm{FIPS}},\phi_{\mathrm{FIPS}})$, using equation 1. A uniformly distributed random number between 0 and 1 was then generated. If that random number was smaller than the fractional part of the calculated N, then $N(E/q,\theta_{\mathrm{FIPS}},\phi_{\mathrm{FIPS}})$ was increased to one plus its integer component. Otherwise, $N(E/q,\theta_{\mathrm{FIPS}},\phi_{\mathrm{FIPS}})$ was reduced to its integer component. Integrating $N(E/q,\theta_{\mathrm{FIPS}},\phi_{\mathrm{FIPS}})$ over all angular bins gave a synthetic E/q distribution, $N(E/q)$, composed of only integer values.

[55] As an example, consider subsonic velocity distributions with properties typical of the subsolar MSH ($n = 100$ cm^{-3}, $T = 2$ MK) and the nightside plasma sheet ($n = 5\,\mathrm{cm}^{-3}$, $T = 10$ MK). Synthetically generated $N(E/q)$ distributions converted to $f(E/q)$ with equation 1 for each case are shown in Figure A1 along with the true $f(E/q)$ distributions. The relative uncertainties at each point are determined from Poisson counting errors. For the subsolar MSH case, which is relatively cold and dense, the lowest E/q steps all contain measured events. Here, $v_{\min}$ corresponds to the velocity of a 100 eV proton. For the plasma sheet case, which is hotter and more sparse, the lowest E/q steps do not contain measured events, leading to a $v_{\min}$ that corresponds to the velocity of a ~250 eV proton. With a known $v_{\min}$, however, the calculation in equations 6 and 7 can be applied for both distributions, leading to recovered plasma parameters of $n = 105\,\mathrm{cm}^{-3}$ and $T = 1.89$ MK, and $n = 5.15\,\mathrm{cm}^{-3}$ and $T = 10.5$ MK, for the MSH and plasma sheet cases, respectively.

[56] Density and temperature values were recovered from sets of synthetic velocity distributions to calculate the uncertainty in the recoveries as a function of the number of measured events in an E/q distribution. Isotropic stationary Maxwell-Boltzmann distributions (equation A1), isotropic drifting Maxwell-Boltzmann distributions (equation A2), and stationary bi-Maxwellian distributions (equation A3) were used for this analysis, i.e.,

$$f(\boldsymbol{v}) = n_{\mathrm{o}}\left(\frac{1}{2\pi}\right)^{3/2}\left(\frac{1}{v_{\mathrm{th}}^3}\right)\exp\left(-\frac{\boldsymbol{v}^2}{2v_{\mathrm{th}}^2}\right), \tag{A1}$$

$$f(\boldsymbol{v}) = n_{\mathrm{o}}\left(\frac{1}{2\pi}\right)^{3/2}\left(\frac{1}{v_{\mathrm{th}}^3}\right)\exp\left(-\frac{(\boldsymbol{v}-\boldsymbol{v}_o)^2}{2v_{\mathrm{th}}^2}\right), \tag{A2}$$

and

$$f(\boldsymbol{v}) = n_{\mathrm{o}}\left(\frac{1}{2\pi}\right)^{3/2}\left(\frac{1}{v_{\mathrm{th},\perp}^2}\right)\left(\frac{1}{v_{\mathrm{th},\parallel}}\right)\exp\left(-\frac{\left(\boldsymbol{v}\bullet\hat{\boldsymbol{b}}\right)^2}{2v_{\mathrm{th},\parallel}^2}-\frac{v^2-\left(\boldsymbol{v}\bullet\hat{\boldsymbol{b}}\right)^2}{2v_{\mathrm{th},\perp}^2}\right). \tag{A3}$$

[57] Here, $v_{\mathrm{th},\parallel} \equiv \sqrt{k_{\mathrm{B}}T_{\parallel}/m}$, $v_{\mathrm{th},\perp} \equiv \sqrt{k_{\mathrm{B}}T_{\perp}/m}$, and $T_{\parallel}$ and $T_{\perp}$ are related to the plasma temperature by the relationship $T = \frac{1}{3}\left(T_{\parallel} + 2T_{\perp}\right)$. The parallel ($\parallel$) and perpendicular ($\perp$) directions are defined with respect to the local direction of the magnetic field defined by unit vector $\hat{\boldsymbol{b}}$. $\mathbf{v_o}$ is the bulk flow velocity vector.

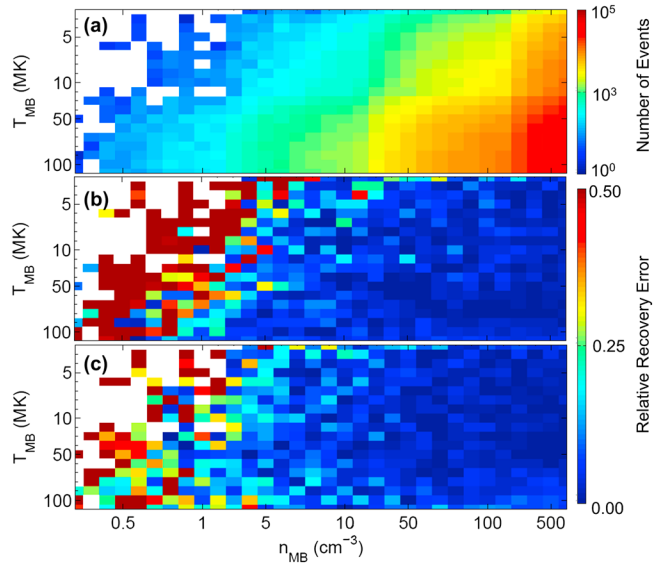

Figure A2. (a) The number of generated events, (b) the relative error in recovered plasma density, and (c) the relative error in recovered plasma temperature for a set of sampled isotropic stationary Maxwell-Boltzmann distributions. White space indicates that no events were generated for a given (n_{MB},T_{MB}) distribution. The recovery errors are observed to decrease with increasing number of measured events.

A1. Isotropic Maxwell-Boltzmann ($\mathbf{v_o} = 0$)

[58] Synthetic proton E/q distributions were generated from stationary ($\mathbf{v_o} = 0$) isotropic ($T_\perp/T_\parallel = 1$) Maxwell-Boltzmann velocity distributions, with densities ranging between 0.1 cm^{-3} and 500 cm^{-3} and temperatures between 1 MK and 100 MK. For each, equations 6 and 7 were used to obtain estimates of the density and temperature, and the relative error between the recovered plasma parameters and the true values was computed. The number of generated events, relative density error, and relative temperature error are shown in Figure A2 as functions of input plasma density and temperature. The recovery error for both density and temperature is observed to decrease with increasing number of measured events, N. Using the synthetic distributions with $N < 500$, we find that the relative density and temperature errors scale as $7.02\,N^{-0.96}$ and $1.10\,N^{-0.64}$, respectively.

A2. Isotropic Maxwell-Boltzmann ($\mathbf{v_o} \neq 0$)

[59] The effect of a nonzero bulk velocity on recovered plasma parameters was determined using a set of drifting isotropic ($T_\perp/T_\parallel = 1$) Maxwell-Boltzmann velocity distributions with a reference density $n = 100$ cm^{-3}, and a reference temperature $T = 2$ MK. These parameters were selected as reference since they will generate $N(E/q)$ distributions with a large number of total measured events. The uncertainties introduced by a bulk plasma flow can then be examined independent of counting error. Here, the bulk flow speed v_o was increased from 0 km/s to 200 km/s, past the plasma thermal speed $v_{th} \sim 130$ km/s, and the direction of the bulk flow varied from ($\theta_{FIPS} = 0°$, $\phi_{FIPS} = 0°$) to ($\theta_{FIPS} = 180°$, $\phi_{FIPS} = 0°$). Since the full range of azimuthal angles is visible to the FIPS sensor in this model, the choice of ϕ_{FIPS} is arbitrary. The relative error in recovered density and temperature as a function of flow direction and magnitude is shown in Figure A3.

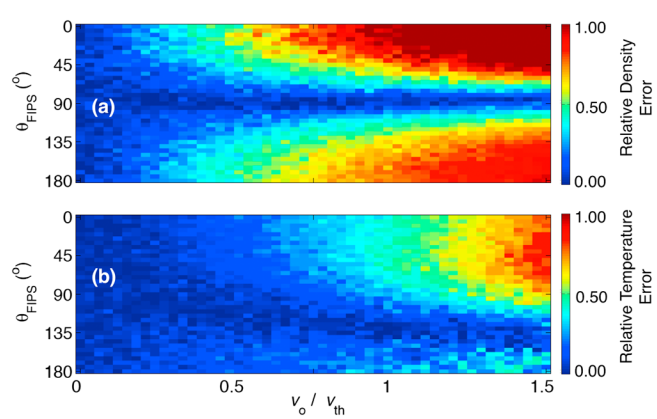

Figure A3. (a) The relative error in recovered plasma density, and (b) the relative error in recovered plasma temperature for a set of sampled isotropic drifting Maxwell-Boltzmann distributions with $n = 100$ cm^{-3} and $T = 2$ MK. The largest errors occur when the flow speed approaches the thermal speed.

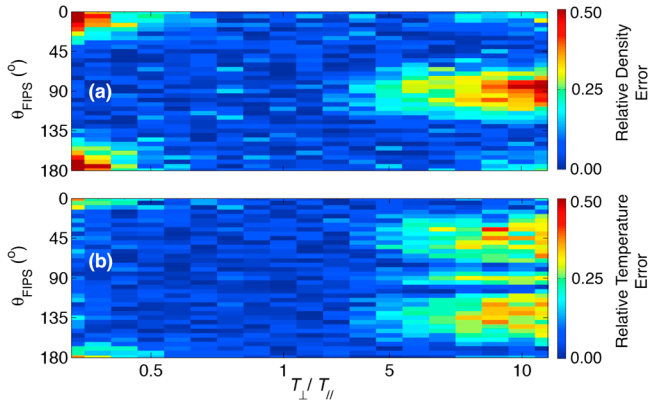

Figure A4. (a) The relative error in recovered plasma density, and (b) the relative error in recovered plasma temperature for a set of sampled stationary bi-Maxwellian distributions with $n = 100\,\mathrm{cm}^{-3}$ and $T = 2$ MK. The largest errors occur when the magnetic field vector is directly parallel or perpendicular to the FIPS boresight direction, i.e., $\theta_{\mathrm{FIPS}} = 0°$ or $\theta_{\mathrm{FIPS}} = 90°$, respectively.

Integration of measured events over the large FIPS FOV serves to substantially mitigate recovery error due to bulk flow, with the smallest errors for low bulk flow speeds or flow directions perpendicular to the FIPS boresight direction.

A3. Bi-Maxwellian ($\mathbf{v_o} = 0$)

[60] The effect of temperature anisotropy on recovered plasma parameters was determined using a set of stationary ($\mathbf{v_o} = 0$) bi-Maxwellian velocity distributions with a reference density $n = 100\,\mathrm{cm}^{-3}$, and a reference temperature $T = 2$ MK. Here, the temperature ratio, $T_\perp/T_\parallel$, was varied between 0.1 and 10, and the direction of the magnetic field in the FIPS frame varied from ($\theta_{\mathrm{FIPS}} = 0°$, $\phi_{\mathrm{FIPS}} = 0°$) to ($\theta_{\mathrm{FIPS}} = 180°$, $\phi_{\mathrm{FIPS}} = 0°$). The relative error in recovered density and temperature as a function of temperature anisotropy and magnetic field direction is shown in Figure A4. For modest temperature anisotropy ($0.5 < T_\perp/T_\parallel < 5$), independent of magnetic field direction, the recovery error is <10%. Integration of measured events over the large FIPS FOV serves to substantially mitigate recovery error due to temperature anisotropy.

Appendix B: Deriving Upstream Solar Wind Dynamic Pressure

[61] The Rankine-Hugoniot jump conditions [*Hudson*, 1970] for a one-dimensional, planar, stationary shock with isotropic upstream and downstream plasmas are:

$$[v_n B_t - v_t B_n] = 0, \tag{B1a}$$

$$\left[p + \frac{B_t^2}{2\mu_o} + \rho v_n^2\right] = 0, \tag{B1b}$$

$$[B_n] = 0, \tag{B1c}$$

$$[\rho v_n] = 0, \tag{B1d}$$

and

$$\left[\rho v_n v_t - \frac{B_n B_t}{\mu_o}\right] = 0, . \tag{B1e}$$

where [] denotes the difference between the downstream and upstream values.

[62] We can combine equations B1a, B1c, B1d, and B1e to eliminate v_t

$$\left[B_t\left(\rho v_n^2 - \frac{B_n^2}{\mu_o}\right)\right] = 0 \tag{B2}$$

and use equation B1d to write

$$\rho_d v_{dn}^2 = \left(\frac{\rho_u}{\rho_d}\right)\rho_u v_{un}^2. \tag{B3}$$

[63] Equations B1b and B2 can then be written as

$$p_d - p_u + \frac{B_{dt}^2}{2\mu_o} - \frac{B_{ut}^2}{2\mu_o} + \rho_u v_{un}^2\left(\left(\frac{\rho_u}{\rho_d}\right) - 1\right) = 0 \tag{B4a}$$

and

$$\rho_u v_{un}^2\left(\left(\frac{\rho_u}{\rho_d}\right)B_{dt} - B_{ut}\right) - \frac{B_n^2}{\mu_o}(B_{dt} - B_{ut}) = 0 \tag{B4b}$$

which can be solved for the upstream dynamic pressure

$$\rho_u v_{un}^2 = \frac{p_d - p_u + \frac{B_{dt}^2}{2\mu_o} - \frac{B_{ut}^2}{2\mu_o}}{\left(1 - \frac{B_{ut}}{B_{dt}}\right)} + \frac{B_n^2}{\mu_o} = \rho_{sw} v_{sw}^2 (\hat{v}_{sw} \cdot \hat{n})^2, \tag{B5}$$

where $\hat{\boldsymbol{v}}_{sw}$ is the dimensionless unit vector corresponding to the solar wind flow direction, here assumed to be radially outward from the Sun. Therefore, under the assumption that the thermal pressure in the solar wind, P_u, is small, we can use the measured magnetic field from MAG and the measured downstream thermal pressure from FIPS to estimate the upstream solar wind dynamic pressure.

[64] **Acknowledgments.** D.J.G. is supported by an appointment to the NASA Postdoctoral Program at Goddard Space Flight Center, administered by Oak Ridge Associated Universities. In addition, this work was supported by the NASA Graduate Student Research Program (J. M. R.) and the MESSENGER mission. The MESSENGER project is supported by the NASA Discovery Program under contracts NAS5-97271 to The Johns Hopkins University Applied Physics Laboratory and NASW-00002 to the Carnegie Institution of Washington.

[65] Masaki Fujimoto thanks Nikolai Erkaev and Stephen Fuselier for their assistance in evaluating this paper.

References

Abraham-Shrauner, B. (1972), Determination of magnetohydrodynamic shock normals, *J. Geophys. Res.*, *77*, 736–739, doi:10.1029/JA077i004p00736.

Anderson, B. J., and S. A. Fuselier (1993), Magnetic pulsations from 0.1 to 4.0 Hz and associated plasma properties in the Earth's subsolar magnetosheath and plasma depletion layer, *J. Geophys. Res.*, *98*, 1461–1479, doi:10.1029/92JA02197.

Anderson, B. J., S. A. Fuselier, S. P. Gary, and R. E. Denton (1994), Magnetic spectral signatures in the Earth's magnetosheath and plasma depletion layer, *J. Geophys. Res.*, *99*, 5877–5891, doi:10.1029/93JA02827.

Anderson, B. J., T. D. Phan, and S. A. Fuselier (1997), Relationships between plasma depletion and subsolar reconnection, *J. Geophys. Res.*, *102*, 9531–9542, doi:10.1029/97JA00173.

Anderson, B. J., M. H. Acuña, D. A. Lohr, J. Scheifele, A. Raval, H. Korth, and J. A. Slavin (2007), The Magnetometer instrument on MESSENGER, *Space Sci. Rev.*, *131*, 417–450, doi:10.1007/s11214-007-9246-7.

Anderson, B. J., C. L. Johnson, H. Korth, M. E. Purucker, R. M. Winslow, J. A. Slavin, S. C. Solomon, R. L. McNutt Jr., J. M. Raines, and T. H. Zurbuchen (2011), The global magnetic field of Mercury from MESSENGER orbital observations, *Science*, *333*, 1859–1862, doi:10.1126/science.1211001.

Andrews, G. B., et al. (2007), The Energetic Particle and Plasma Spectrometer instrument on the MESSENGER spacecraft, *Space Sci. Rev.*, *131*, 523–556, doi:10.1007/s11214-007-9272-5.

Baker, D. N., et al. (2013), Solar wind forcing at Mercury: WSA-ENLIL model results, *J. Geophys. Res. Space Physics*, *118*, 45–57, doi:10.1029/2012JA018064.

Berchem, J., J. Raeder, and M. Ashour-Abdalla (1995), Magnetic flux ropes at the high-latitude magnetopause, *Geophys. Res. Lett.*, *22*, 1189–1192, doi:10.1029/95GL01014.

Bertucci, C., et al. (2003a), Magnetic field draping enhancement at the Martian magnetic pileup boundary from Mars Global Surveyor observations, *Geophys. Res. Lett.*, *30*(2), 1099, doi:10.1029/2002GL015713.

Bertucci, C., C. Mazelle, J. A. Slavin, C. T. Russell, and M. H. Acuña (2003b), Magnetic field draping enhancement at Venus: Evidence for a magnetic pileup boundary, *Geophys. Res. Lett.*, *30*(17), 1876, doi:10.1029/2003GL017271.

Bertucci, C., C. Mazelle, M. H. Acuña, C. T. Russell, and J. A. Slavin (2005), Structure of the magnetic pileup boundary at Mars and Venus, *J. Geophys. Res.*, *110*, A01209, doi:10.1029/2004JA010592.

Coleman, I. J. (2005), A multi-spacecraft survey of magnetic field line draping in the dayside magnetosheath, *Ann. Geophys.*, *23*, 885–900.

Coleman, I. J., M. Pinnock, and A. S. Rodger (2000), The ionospheric footprint of antiparallel merging regions on the dayside magnetopause, *Ann. Geophys.*, *18*, 511–516.

Crooker, N. U., T. E. Eastman, and G. S. Stiles (1979), Observations of plasma depletion in the magnetosheath at the dayside magnetopause, *J. Geophys. Res.*, *84*, 869–874, doi:10.1029/JA084iA03p00869.

Cummings, W. D., and P. J. Coleman Jr. (1968), Magnetic fields in the magnetopause and vicinity at synchronous altitude, *J. Geophys. Res.*, *73*, 5699–5718, doi:10.1029/JA073i017p05699.

Denton, R. E., and J. G. Lyon (2000), Effect of pressure anisotropy on the structure of a two-dimensional magnetosheath, *J. Geophys. Res.*, *105*, 7545–7556, doi:10.1029/1999JA000360.

Denton, R. E., B. J. Anderson, S. P. Gary, and S. A. Fuselier (1994), Bounded anisotropy fluid model for ion temperatures, *J. Geophys. Res.*, *99*, 11,225–11,241.

DiBraccio, G. A., J. A. Slavin, S. A. Boardsen, B. J. Anderson, H. Korth, T. H. Zurbuchen, J. M. Raines, D. N. Baker, R. L. McNutt Jr., and S. C. Solomon (2013), MESSENGER observations of magnetopause structure and dynamics at Mercury, *J. Geophys. Res. Space Physics*, *118*, 997–1008, doi:10.1002/jgra.50123.

Erkaev, N. V., C. J. Farrugia, and H. K. Biernat (2003), The role of the magnetic barrier in the solar wind-magnetosphere interaction, *Planet. Space Sci.*, *51*, 745–755.

Fairfield, D. H. (1979), On the average configuraton of the geomagnetic tail, *J. Geophys. Res.*, *84*, 1950–1958, doi:10.1029/JA084iA05p01950.

Farrugia, C. J., N. V. Erkaev, H. K. Biernat, and L. F. Burlaga (1995), Anomalous magnetosheath properties during Earth passage of an interplanetary magnetic cloud, *J. Geophys. Res.*, *100*, 19,245–19,257, doi:10.1029/95JA01080.

Farrugia, C. J., N. V. Erkaev, H. K. Biernat, G. R. Lawrence, and R. C. Elphic (1997), Plasma depletion layer model for low Alfvén Mach number: Comparison with ISEE observations, *J. Geophys. Res.*, *102*, 11,315–11,324, doi:10.1029/97JA00410.

Feldman, W. C., J. R. Asbridge, S. J. Bame, M. D. Montgomery, and S. P. Gary (1975), Solar wind electrons, *J. Geophys. Res.*, *80*, 4181–4196, doi:10.1029/JA080i031p04181.

Fuselier, S. A., D. M. Klumpar, E. G. Shelley, B. J. Anderson, and A. J. Coates (1991), He^{2+} and H^{+} dynamics in the subsolar magnetosheath and plasma depletion layer, *J. Geophys. Res.*, *96*, 21,095–21,104, doi:10.1029/91JA02145.

Fuselier, S. A., B. J. Anderson, S. P. Gary, and R. E. Denton (1994), Inverse correlations between the ion temperature anisotropy and plasma beta in the Earth's quasi-parallel magnetosheath, *J. Geophys. Res.*, *99*, 14,931–14,936, doi:10.1029/94JA00865.

Gary, S. P., M. E. McKean, and D. Winske (1993), Ion cyclotron anisotropy instabilities in the magnetosheath: Theory and simulations, *J. Geophys. Res.*, *98*, 3963–3971, doi:10.1029/92JA02585.

Gary, S. P., J. Wang, D. Winske, and S. A. Fuselier (1997), Proton temperature anisotropy upper bound, *J. Geophys. Res.*, *102*, 27,159–27,169, doi:10.1029/97JA01726.

Gershman, D. J., T. H. Zurbuchen, L. A. Fisk, J. A. Gilbert, J. M. Raines, B. J. Anderson, C. W. Smith, H. Korth, and S. C. Solomon (2012), Solar wind alpha particles and heavy ions in the inner heliosphere observed with MESSENGER, *J. Geophys. Res.*, *117*, A00M02, doi:10.1029/2012JA017829.

Hesterberg T. C., D. S. Moore, S. Monaghan, A. Clipson, R. Epstein, B. A. Craig, and G. P. McCabe (2010), Bootstrap methods and permutation tests, in *Introduction to the Practice of Statistics*, 7th ed., edited by D. S. Moore, G. P. McCabe, and B. A. Craig, 70 pp., W. H. Freeman, New York.

Holzer, R. E., and J. A. Slavin (1978), Magnetic flux transfer associated with expansions and contractions of the dayside magnetosphere, *J. Geophys. Res.*, *83*, 3831–3839, doi:10.1029/JA083iA08p03831.

Hudson, P. D. (1970), Discontinuities in an anisotropic plasma and their identification in the solar wind, *Planet. Space Sci.*, *18*, 1611–1622.

Joy, S. P., M. G. Kivelson, R. J. Walker, K. K. Khurana, C. T. Russell, and W. R. Paterson (2006), Mirror mode structures in the Jovian magnetosheath, *J. Geophys. Res.*, *111*, A12212, doi:10.1029/2006JA011985.

Korth, H., B. J. Anderson, J. M. Raines, J. A. Slavin, T. H. Zurbuchen, C. L. Johnson, M. E. Purucker, R. M. Winslow, S. C. Solomon, and R. L. McNutt Jr. (2011), Plasma pressure in Mercury's equatorial magnetosphere derived from MESSENGER Magnetometer observations, *Geophys. Res. Lett.*, *38*, L22201, doi:10.1029/2011GL049451.

Le, G., C. T. Russell, and J. T. Gosling (1994), Structure of the magnetopause for low Mach number and strongly northward interplanetary magnetic field, *J. Geophys. Res.*, *99*, 23,723–23,734, doi:10.1029/94JA02182.

Le, G., C. T. Russell, J. T. Gosling, and M. F. Thomsen (1996), ISEE observations of low-latitude boundary layer for northward interplanetary magnetic field: Implications for cusp reconnection, *J. Geophys. Res.*, *101*, 27,239–27,249, doi:10.1029/96JA02528.

Lees, L. (1964), Interaction between the solar plasma wind and the geomagnetic cavity, *AIAA J.*, *2*, 1576–1582.

Liu, Y., J. D. Richardson, J. W. Belcher, J. C. Kasper, and R. M. Skoug (2006a), Plasma depletion and mirror waves ahead of interplanetary coronal mass ejections, *J. Geophys. Res.*, *111*, A09108, doi:10.1029/2006JA011723.

Liu, Y., J. D. Richardson, J. Belcher, C. Wang, Q. Hu, and J. C. Kasper (2006b), Constraints on the global structure of magnetic clouds: Transverse size and curvature, *J. Geophys. Res.*, *111*, A12S03, doi:10.1029/2006JA011890.

Luhmann, J. G. (1986), The solar wind interaction with Venus, *Space Sci. Rev.*, *44*, 241–306.

Lyon, J. G. (1994), MHD simulations of the magnetosheath, *Adv. Space. Sci.*, *147*, 21–28.

Maksimovic, M. V., V. Pierrard, and P. Riley (1997), Ulysses electron distributions fitted with kappa functions, *Geophys. Res. Lett.*, *24*, 1151–1154.

Maksimovic, M. V., et al. (2005), Radial evolution of the electron distribution functions in the fast solar wind between 0.3 and 1.5 AU, *J. Geophys. Res.*, *110*, A09104, doi:10.1029/2005JA011119.

McAdams, J. V., et al. (2012), MESSENGER at Mercury: From orbit insertion to first extended mission, paper given at the *63rd International Astronautical Congress*, paper IAC-12-C1.5.6, 11 pp., Naples, Italy, October 1–5.

Midgley, J. E., and L. Davis Jr. (1963), Calculation by a moment technique of the perturbation of the geomagnetic field by the solar wind, *J. Geophys. Res.*, *68*, 5111–5123, doi:10.1029/JZ068i018p05111.

Moretto, T., D. G. Sibeck, B. Lavraud, K. J. Trattner, H. Rème, and A. Balogh (2005), Flux pile-up and plasma depletion at the high latitude dayside magnetopause during southward interplanetary magnetic field: A Cluster event study, *Ann. Geophys.*, *23*, 2259–2264.

Nabert, C., K.-H. Glassmeier, and F. Plaschke (2013), A new method for solving the MHD equations in the magnetosheath, *Ann. Geophys.*, *31*, 419–437.

Nieves-Chinchilla, T., and A. F. Viñas (2008), Solar wind electron distribution functions inside magnetic clouds, *J. Geophys. Res.*, *113*, A02105, doi:10.1029/2007JA012703.

Øieroset, M., D. L. Mitchell, T. D. Phan, P. R. Lin, D. H. Crider, and M. H. Acuña (2004), The magnetic field pile-up and density depletion in

the Martian magnetosheath: A comparison with the plasma depletion layer upstream of the Earth's magnetopause, *Space Sci. Rev.*, *111*, 185–202, doi:10.1023/B:SPAC.0000032715.69695.9c.

Onsager, T. G., J. D. Scudder, M. Lockwood, and C. T. Russell (2001), Reconnection at the high-latitude magnetopause during northward interplanetary magnetic field conditions, *J. Geophys. Res.*, *106*, 25,467–25,488, doi:10.1029/2000JA000444.

Paschmann, G., W. Baumjohann, N. Sckopke, T. D. Phan, and H. Lühr (1993), Structure of the dayside magnetopause for low magnetic shear, *J. Geophys. Res.*, *98*, 13,409–13,422, doi:10.1029/93JA00646.

Phan, T. D., G. Paschmann, W. Baumjohann, N. Sckopke, and H. Lühr (1994), The magnetosheath region adjacent to the dayside magnetopause: AMPTE/IRM observations, *J. Geophys. Res.*, *99*, 121–141, doi:10.1029/93JA02444.

Phan, T. D., et al. (1997), Low-latitude dusk flank magnetosheath, magnetopause, and boundary layer for low magnetic shear: Wind observations, *J. Geophys. Res.*, *102*, 19,883–19,895, doi:10.1029/97JA01596.

Phan, T., et al. (2003), Simultaneous Cluster and IMAGE observations of cusp reconnection and auroral proton spot for northward IMF, *Geophys. Res. Lett.*, *30*(10), 1509, doi:10.1029/2003GL016885.

Pilipp, W. G., H. Miggenrieder, M. D. Montgomery, K.-H. Mühlhaüser, H. Rosenbauer, and R. Schwenn (1987), Unusual electron distribution functions in the solar wind derived from the Helios plasma experiment: Double-strahl distributions and distributions with an extremely anisotropic core, *J. Geophys. Res.*, *92*, 1093–1101.

Raines, J. M., J. A. Slavin, T. H. Zurbuchen, G. Gloeckler, B. J. Anderson, D. N. Baker, H. Korth, S. M. Krimigis, and R. L. McNutt Jr. (2011), MESSENGER observations of the plasma environment near Mercury, *Planet. Space Sci.*, *59*, 2004–2015, doi:10.1016/j.pss.2011.02.004.

Schwartz, S. J. (1998), Shock and discontinuity normals, Mach numbers, and related parameters, in *Analysis Methods for Multi-Spacecraft Data*, edited by G. Paschmann and P. Daly, pp. 249–270 , International Space Science Institute, Bern, Switzerland.

Scurry, L., C. T. Russell, and J. T. Gosling (1994), Geomagnetic activity and the beta dependence of the dayside reconnection rate, *J. Geophys. Res.*, *99*, 14,811–14,814, doi:10.1029/94JA00794.

Siscoe, G. L., N. U. Crooker, G. M. Erickson, B. U. O. Sonnerup, N. C. Maynard, J. A. Schoendorf, K. D. Siebert, D. R. Weimer, W. W. White, and G. R. Wilson (2002), MHD properties of magnetosheath flow, *Planet. Space Sci.*, *50*, 461–471.

Skoug, R. M., W. C. Feldman, J. T. Gosling, D. J. McComas, and C. W. Smith (2000), Solar wind electron characteristics inside and outside coronal mass ejections, *J. Geophys. Res.*, *105*, 23,069–23,084.

Slavin, J. A., and R. E. Holzer (1979), The effect of erosion on the solar wind stand-off distance at Mercury, *J. Geophys. Res.*, *84*, 2076–2082, doi:10.1029/JA084iA05p02076.

Slavin, J. A., R. C. Elphic, C. T. Russell, F. L. Scarf, J. H. Wolfe, J. D. Mihalov, D. S. Intriligator, L. H. Brace, H. A. Taylor Jr., and R. E. Daniell Jr. (1980), The solar wind interaction with Venus: Pioneer Venus observations of bow shock location and structure, *J. Geophys. Res.*, *85*, 7625–7641.

Slavin, J. A., E. J. Smith, P. R. Gazis, and J. D. Mihalov (1983), A Pioneer-Voyager study of the solar wind interactions with Saturn, *Geophys. Res. Lett.*, *10*, 9–12.

Slavin, J. A., et al. (2009), MESSENGER observations of magnetic reconnection in Mercury's magnetosphere, *Science*, *324*, 606–610, doi:10.1126/science.1172011.

Slavin, J. A., et al. (2010), MESSENGER observations of extreme loading and unloading of Mercury's magnetic tail, *Science*, *329*, 665–668, doi:10.1126/science.1188067.

Slavin, J. A., et al. (2012), MESSENGER observations of a flux-transfer-event shower at Mercury, *J. Geophys. Res.*, *117*, A00M06, doi:10.1029/2012JA017926.

Solomon, S. C., et al. (2001), The MESSENGER mission to Mercury: Scientific objectives and implementation, *Planet. Space Sci.*, *49*, 1445–1465.

Song, P., C. T. Russell, J. T. Gosling, M. Thomsen, and R. C. Elphic (1990), Observations of the density profile in the magnetosheath near the stagnation streamline, *Geophys. Res. Lett.*, *17*, 2035–2038.

Song, P., C. T. Russell, R. J. Fitzenreiter, J. T. Gosling, M. F. Thomsen, D. G. Mitchell, S. A. Fuselier, G. K. Parks, R. R. Anderson, and D. Hubert (1993), Structure and properties of the subsolar magnetopause for northward interplanetary magnetic field: Multiple-instrument particle observations, *J. Geophys. Res.*, *98*, 11,319–11,337, doi:10.1029/93JA00606.

Southwood, D. J., and M. G. Kivelson (1992), On the form of the flow in the magnetosheath, *J. Geophys. Res.*, *97*, 2873–2879, doi:10.1029/91JA02446.

Southwood, D. J., and M. G. Kivelson (1995), Magnetosheath flow near the subsolar magnetopause: Zwan-Wolf and Southwood-Kivelson theories reconciled, *Geophys. Res. Lett.*, *22*, 3275–3278.

Spreiter, J. R., A. L. Summers, and A. Y. Alksne (1966), Hydrodynamic flow around the magnetosphere, *Planet. Space Sci.*, *14*, 223–253.

Viñas, A. F., and C. Gurgiolo (2009), Spherical harmonic analysis of particle velocity distribution function: Comparison of moments and anisotropies using Cluster data, *J. Geophys. Res.*, *114*, A01105, doi:10.1029/2008JA013633.

Violante, L., M. B. B. Cattaneo, G. Moreno, and J. D. Richardson (1995), Observations of mirror waves and plasma depletion layer upstream of Saturn's magnetopause, *J. Geophys. Res.*, *100*, 12,047–12,055, doi:10.1029/94JA02703.

Wang, Y. L., J. Raeder, C. T. Russell, T. D. Phan, and M. Manapat (2003), Plasma depletion layer: Event studies with a global model, *J. Geophys. Res.*, *108*(A1), 1010, doi:10.1029/2002JA009281.

Wang, Y. L., J. Raeder, and C. T. Russell (2004), Plasma depletion layer: Magnetosheath flow structure and forces, *Ann. Geophys.*, *22*, 1001–1017.

Wang, C.-P., M. Gkioulidou, L. R. Lyons, and V. Angelopoulos (2012), Spatial distributions of the ion to electron temperature ratio in the magnetosheath and plasma sheet, *J. Geophys. Res.*, *117*, A08215, doi:10.1029/2012JA017658.

Winslow, R. M., C. L. Johnson, B. J. Anderson, H. Korth, J. A. Slavin, M. E. Purucker, and S. C. Solomon (2012), Observations of Mercury's northern cusp region with MESSENGER's Magnetometer, *Geophys. Res. Lett.*, *39*, L08112, doi:10.1029/2012GL051472.

Winslow, R. M., B. J. Anderson, C. L. Johnson, J. A. Slavin, H. Korth, M. E. Purucker, D. N. Baker, and S. C. Solomon (2013), Mercury's magnetopause and bow shock from MESSENGER Magnetometer observations, *J. Geophys. Res. Space Physics*, *118*, 2213–2227, doi:10.1002/jgra.50237.

Zhang, T. L., J. G. Luhmann, and C. T. Russell (1991), The magnetic barrier at Venus, *J. Geophys. Res.*, *96*, 11,145–11,153, doi:10.1029/91JA00088.

Zurbuchen, T. H., et al. (2011), MESSENGER observations of the spatial distribution of planetary ions near Mercury, *Science*, *333*, 1862–1865, doi:10.1126/science.1211302.

Zwan, B. J., and R. A. Wolf (1976), Depletion of solar wind plasma near a planetary boundary, *J. Geophys. Res.*, *81*, 1636–1648, doi:10.1029/JA081i010p01636.